Journal of Nuclear Materials 627 (2026) 156624

Contents lists available at ScienceDirect

Journal of Nuclear Materials

journal homepage: www.elsevier.com/locate/jnucmat

Helium doping and ion-solid interactions in $A_2Zr_2O_7$ (A = Gd, Lu) weberites: Ab initio insights

Xiaoyi Xia[a,b,c], Haowen Guo[a,b,c], Rongrong Gao[a,b,c], Yue Xia[d,**], Chenguang Liu[a,b,c,*], Qing Peng[e], Yuhong Li[f], Fei Gao[g]

[a] College of Nuclear Equipment and Nuclear Engineering, Yantai University, Yantai 264005, Shandong, China
[b] Shandong Key Laboratory of Special Metallic Materials for Nuclear Equipment, Yantai University, Yantai 264005, Shandong, China
[c] Yantai Key Laboratory of Advanced Nuclear Energy Materials and Irradiation Technology, Yantai University, Yantai 264005, Shandong, China
[d] Key Laboratory of Advanced Nuclear Energy Design and Safety, Ministry of Education, University of South China, Hengyang 421001, Hunan, China
[e] Power and Mechanical Engineering, Wuhan University, Wuhan 430072, China
[f] School of Nuclear Science &Technology, Lanzhou University, Lanzhou 730000, China
[g] Nuclear Engineering & Radiological Sciences, University of Michigan, Ann Arbor, MI 48109, USA

ARTICLE INFO

Keywords:
First-principles
Helium
Ab initio molecular dynamics
Weberite
Irradiation resistance

ABSTRACT

Radiation-induced displacement damage and helium (He) accumulation from α-decay are key factors driving structural degradation and amorphization in nuclear waste forms, directly impacting the long-term stability of radionuclide immobilization materials. The present investigation applies first-principles method to analyze the influence of He atom doping on the structural and electronic features of $A_2Zr_2O_7$ (A = Gd, Lu) weberites. Furthermore, ab initio molecular dynamics (AIMD) simulations are utilized to study low-energy recoil events. He atoms preferentially occupy octahedral interstitial sites, which causes lattice expansion and significantly reduces cation antisite defect formation energies, thereby accelerates order-to-disorder phase transitions. The ⟨Zr-O⟩ bond plays a dominant role in irradiation resistance in He-$Lu_2Zr_2O_7$ weberite, whereas both ⟨Gd-O⟩ and ⟨Zr-O⟩ bonds collectively influence radiation tolerance in He-$Gd_2Zr_2O_7$ weberite. AIMD simulations of low-energy recoil events reveal the pronounced anisotropy in threshold displacement energy (E_d) of weberites, with anion disordering playing a crucial role in the displacement processes. A-site cations exhibit higher displacement susceptibility than Zr cations, and $Gd_2Zr_2O_7$ weberite demonstrates a greater propensity for cation antisite defect formation under low-energy irradiation, consistent with its lower defect formation energies. Compared to $Lu_2Zr_2O_7$ weberite and $Gd_2Zr_2O_7$ pyrochlore, $Gd_2Zr_2O_7$ weberite exhibits lower threshold displacement energies, indicating a higher susceptibility to order-disorder transitions. An integrated analyses of defect energetics and displacement mechanisms suggests that $Gd_2Zr_2O_7$ weberite possesses superior radiation resistance.

1. Introduction

High-level nuclear waste forms must endure extreme conditions, including intense radiation, high temperatures, and complex crustal stresses. Consequently, these materials require exceptional irradiation resistance, thermal stability, and mechanical durability. The complex oxide matrices such as perovskites, zirconolites and pyrochlores are among the most promising candidates for immobilizing radionuclides, offering long-term stability for deep geological repositories [1]. Among these complex oxides, pyrochlore has drawn significant research interest due to its outstanding resistance to irradiation, as well as its thermal and mechanical stability. The distinctive attributes of pyrochlore render it particularly appropriate for multiple technological implementations, such as thermal barrier coatings [2,3], stabilization agents in nuclear fuel matrices [4], solid electrolytes [5–7], and nuclear waste immobilization matrices [8–11]. For $A_2B_2O_7$ pyrochlores, the cation radius ratio (r_A/r_B) serves as a principal indicator for assessing structural integrity, where A and B correspond to specific cationic coordination sites [12]. Stability of the pyrochlore structure is maintained within the radius ratio interval of 1.46–1.78, whereas ratios below 1.46 predominantly

---

* Corresponding author at: College of Nuclear Equipment and Nuclear Engineering, Yantai University, Yantai 264005, Shandong, China.
** Corresponding author.
E-mail addresses: xiay92@126.com (Y. Xia), liuchg@ytu.edu.cn (C. Liu).

https://doi.org/10.1016/j.jnucmat.2026.156624
Received 3 May 2025; Received in revised form 13 February 2026; Accepted 25 March 2026

induce structural reorganization into fluorite-type phases [13].Some pyrochlores undergo phase transitions from an ordered to a disordered (O-D) or amorphous (O-A) state under irradiation [14]. The likelihood of these transitions is closely related to the energetic cost of cation disordering within the pyrochlore lattice [14,15]. The O-D phase transition involve the exchange of A and B cations, along with the random redistribution of oxygen vacancies caused by anion Frenkel defects [14]. The extent of cation disorder significantly influences the material's functional properties and its resistance to amorphization [15].

Recent investigation using neutron scattering analysis has shown that there is the local atomic arrangement in disordered pyrochlore, which can be effectively described by the short-range order of the weberite (WB) model [16,17] This structure exhibits an intermediate level of order between the ordered pyrochlore (PY) phase and the disordered fluorite (DF) phase [18]. Zhao *et al.* [19] conducted first-principles calculations to study the local structure in zirconate pyrochlore, revealing that the migration of O_{48f} ions to the nearest intrinsic 8*a* vacancies facilitates the formation of a local network structure. Systematic studies on $A_2B_2O_7$ (A = Lu, La; B = Zr, Hf, Sn, Ti) compounds demonstrate that reduced A-site cation radii enhance structural stability compared to the pyrochlore configuration [20]. The formation enthalpy calculations for pyrochlore, weberite, and defective fluorite phases in the $Ln_2B_2O_7$ (B = Ti, Sn, Hf, Zr) system revealed, that when doped with Dy and Gd, the weberite structure of $Ln_2Hf_2O_7$ and $Ln_2Zr_2O_7$ is more stable than the pyrochlore structure [17]. The computational findings demonstrate that local structural variation critically governs the stability of pyrochlore-structured materials. Zirconate pyrochlore is considered a primary candidate material for immobilizing long-lived actinides [21,22]. $Gd_2Zr_2O_7$ weberite is more effective in immobilizing long-lived actinides compared to $Gd_2Zr_2O_7$ pyrochlore and $Gd_2Zr_2O_7$ quasi-WB [23]. Recent studies on the local site disorder in $Ln_2Zr_2O_7$ demonstrated that as the A-site cation transitions from La to Sm, the material predominantly adopts a PY structure. Conversely, when the A-site cation changes from Gd to Lu, the WB structure becomes more favorable [19]. To gain deeper insight into the structural and physical characteristics associated with these distinct configurations, $Gd_2Zr_2O_7$ and $Ln_2Zr_2O_7$ representative WB-type compounds at opposite ends of the compositional spectrum have been selected for comprehensive investigation via first-principles calculations. This study aims to provide deeper insights into their potential applications in nuclear waste immobilization.

A significant challenge in actinide-containing nuclear waste forms is He accumulation, a byproduct of α-decay. He atoms tend to occupy octahedral interstitial sites, leading to lattice distortions and modifications in bonding characteristics, as observed in $Y_2Ti_2O_7$ pyrochlore [24–26]. At low concentrations, He induces minimal lattice swelling with little impact on mechanical properties. However, this effect reduces the energy barrier for cation antisite defect formation, thereby facilitating structural disordering processes. It is of interest to understand how He atoms affect the structural and electronic effects of He incorporation in $A_2Zr_2O_7$ (A = Gd, Lu) weberites, thus, further refining the assessment of its irradiation resistance.

Irradiation-induced displacement damage, caused by recoil nuclei generated during α-decay, can result in varying degrees of structural degradation and eventual amorphization in pyrochlore [27,28]. However, the studies on weberite under such conditions remain limited. The threshold displacement energy (E_d), a fundamental metric in radiation tolerance evaluation, quantifies the minimum kinetic energy required to dislodge lattice-bound atoms and establish persistent crystalline defects [29–31]. Due to the anisotropic nature and fixed sublattice structure of weberites, the experimental determination of E_d remains challenging, and it is difficult to generate single defects in irradiation experiments [32]. Consequently, computational methods are increasingly relied upon for these assessments. Molecular dynamics (MD) has been proven effective for predicting E_d and analyzing recoil events in materials [32–34]. However, classical molecular dynamics (CMD) simulations are inherently dependent on empirical interatomic potentials, which are the primary source of error in E_d calculations [35]. These errors often stem from neglecting partial charge transfer effects, leading to significant inaccuracies. In contrast, AIMD which derives interatomic forces directly from electronic structure calculations, eliminates these inaccuracies at the cost of higher computational expense. Recent studies have successfully employed AIMD methods to determine the cation displacement threshold energies in pyrochlore structures such as $Y_2Ti_2O_7$ [36], $Gd_2Zr_2O_7$ [37], and $Y_4Zr_3O_{12}$ [38], as well as in materials like SiC [35,39] and GaN [34]. These studies have shown that E_d exhibit pronounced anisotropy and is strongly influenced by the direction of the incident particle.

In this work, we conducted AIMD simulations to calculate the displacement threshold energies for cation (A), zirconium (Zr), and oxygen (O) along three principal crystallographic directions in $A_2Zr_2O_7$ (A = Gd, Lu) weberite. The resulting defects and their formation mechanisms were systematically analyzed, and the findings were compared with those from pyrochlore structures to gain deeper insights into their radiation tolerance.

2. Computational details

The Vienna Ab-initio Simulation Package (VASP) implemented with density functional theory (DFT) [40,41] was employed for all quantum mechanical computations. Ion-electron interactions were modeled through the projector augmented wave (PAW) [42,43], while the Perdew-Burke-Ernzerhof (PBE) functional within the generalized gradient approximation (GGA) [44] accounted for exchange-correlation effects. The electronic configurations for Gd, Lu, Zr, and O are $5p^6 5d^1 6s^2$, $5p^6 5d^1 6s^2$, $4s^2 4p^6 4d^2 5s^2$ and $2s^2 2p^4$, respectively. For rare-earth cations (Gd, Lu), the 4f electrons were treated using the f-in-core approach, in which the 4f states are incorporated into the pseudopotential core. This treatment has been demonstrated in previous comparative studies on $A_2Zr_2O_7$ (A = Nd, Sm, Gd, and Yb) pyrochlores to yield structural and energetic properties in close agreement with experimental data and with the DFT+U method [45–47]. Explicit inclusion of 4f electrons was found to have only a marginal influence on the structural and electronic properties, while the f-in-core treatment offers computational efficiency and has been widely adopted in prior work on Gd- and Lu-containing pyrochlores and weberites [19,47]. Adopting this approach therefore ensures both accuracy and consistency with the established literature.

To capture the characteristic short-range order (SRO) of defect fluorite phases, the weberite structure was modeled with partial cation disorder following the approach reported in previous studies [17,19,48]. Specifically, weberite has an orthorhombic structure with four formula units per unit cell. Taking $Gd_2Zr_2O_7$ weberite as an example, Gd cations occupy the 4b and 8 g sites, while Zr cations are positioned at the 4a and 8 g sites. 50% of the Gd and Zr cations were fully ordered, occupying the 4b (Gd) and 4a (Zr) lattice sites with 8-fold and 6-fold coordination, respectively. The remaining 50% of the Gd and Zr cations were randomly distributed over the 8 g sites, where they adopt 7-fold coordination. Oxygen anions are distributed randomly among the 16 h and three 4c sites, whereas the fourth 4c site is occupied by an intrinsic vacancy. To represent the cation disorder statistically, a special quasi-random structure (SQS) [49] approach was employed, in which eight distinct cation sites were used to generate the disordered configuration. This model effectively reproduces the pair-correlation functions of a fully random alloy up to the third-nearest neighbor shell within the 44-atom (four formula units) supercell, ensuring a representative description of cation disorder while remaining computationally tractable for electronic structure analysis. This configuration preserves the essential coordination environments and oxygen sublattice distortions observed in experimental weberite like regions, while enabling a computationally tractable model for first-principles calculations. This is consistent with the approach of Zhao *et al.* [19]. Fig. 1 (a) shows the lattice structure of the $Gd_2Zr_2O_7$ weberite unit cell, which consists of 44

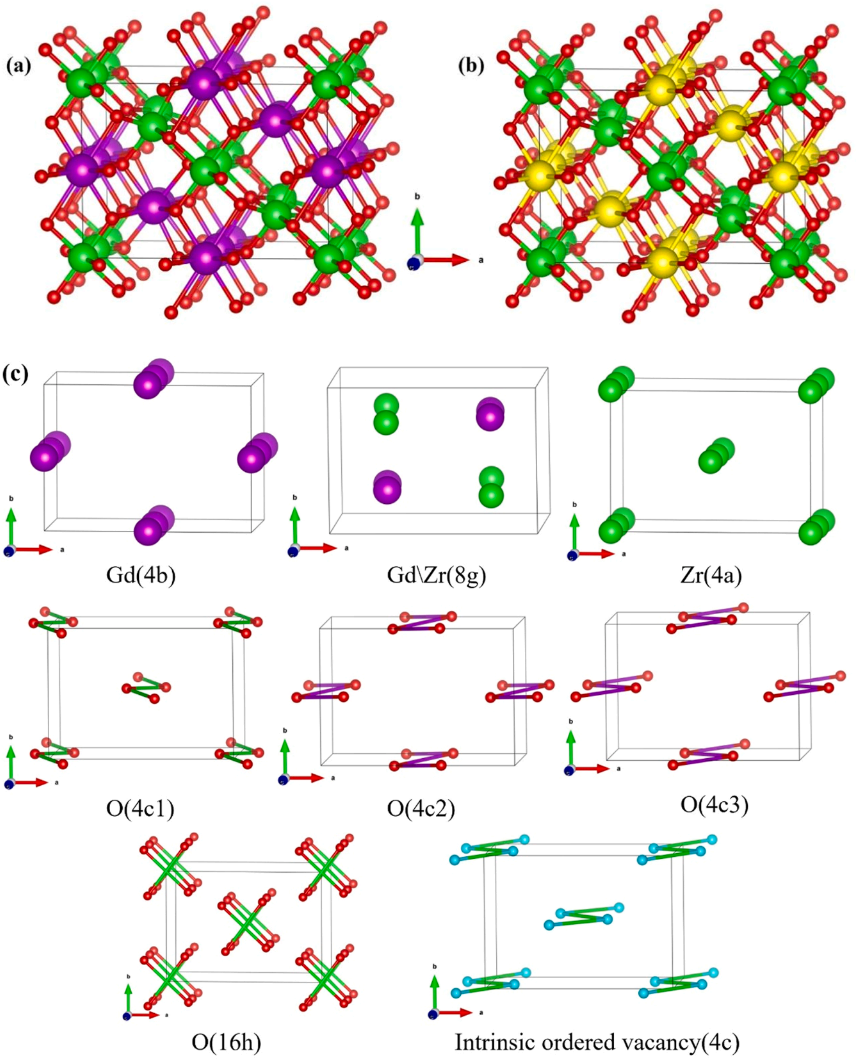

Fig. 1. (a) $Gd_2Zr_2O_7$ weberite and (b) $Lu_2Zr_2O_7$ weberite unit cell contain 44 atoms. (c) Wyckoff position occupied by each atom. The purple, yellow, green, red and blue spheres represent Gd, Lu, Zr, O and intrinsic ordered vacancy respectively.

atoms. Similarly, the unit cell of $Lu_2Zr_2O_7$ weberite is shown in Fig. 1 (b).

In this structure, Zr atoms at the 4a site exhibit 6-flod coordination, forming polyhedral units with two O_{4c1} and four O_{16h} atoms. Gd and Lu atoms at the 4b position are 8-flod coordinated, forming polyhedra with two O_{4c2}, two O_{4c3}, and four O_{16h} atoms. The Zr and Gd atoms located at the 8 g site each exhibit 7-fold coordination, bonding with one O atom from each of the O_{4c1}, O_{4c2}, and O_{4c3} sites, along with four O atoms from the O_{16h} sites, forming distinct polyhedral units. In the unit cell of $Gd_2Zr_2O_7$ weberite (Fig. 1 (c)), there are four distinct positions for O atoms: O_{16h}, O_{4c1}, O_{4c2}, and O_{4c3}. The O_{16h} sites are occupied by 16 oxygen atoms, while the remaining O sites (O_{4c1}, O_{4c2}, O_{4c3}) each contain four oxygen atoms.

In this work, different atomic models are adopted for $A_2Zr_2O_7$ ($A =$ Gd, Lu) weberite structures depending on the target physical properties. Specifically, a 176-atom weberite supercell is employed for AIMD simulations and formation enthalpy calculations, whereas all other first-principles calculations are performed using the 44-atom primitive cell. The use of the 176-atom supercell in AIMD simulations is essential to mitigate spurious interactions between periodic images during the simulation of displacement cascade events triggered by primary knock-on atoms (PKAs). By enlarging the simulation domain, the interference from periodic boundary conditions is effectively suppressed, thereby ensuring the physical fidelity of the cascade evolution. In addition, the 176-atom supercell is also adopted for formation enthalpy calculations. This choice is necessitated by the complex atomic site occupancy and the lower structural symmetry of the weberite phase. This ensures that accurate thermodynamic stability energies are obtained during the relaxation process, minimizing errors arising from periodic boundary conditions. For the remaining first-principles calculations, the 44-atom primitive cell is utilized, as it is physically equivalent to larger-scale models when addressing these specific physical properties [19]. This strategy provides an optimal balance between computational efficiency and accuracy, enabling the use of a more advanced DFT setup while maintaining reliable predictive capability.

For first-principles calculations, the 44-atom primitive cells of $A_2Zr_2O_7$ ($A =$ Gd, Lu) weberites were employed for geometric optimization and electronic-structure characterization, except in the formation enthalpy calculations. This choice was made because the primitive cells preserve the intrinsic crystallographic symmetry as well as the relative cation/anion arrangements within the sublattices, thereby providing an accurate and computationally efficient description for these properties. In addition, the 44-atom models were used to investigate the site preference and aggregation behavior of incorporated He atoms, together with the corresponding effects of He on the local geometric distortion, electronic properties, and cation disorder. All static first-principles calculations based on the 44-atom primitive cells were performed using a $3 \times 4 \times 4$ Monkhorst-Pack k-point mesh and a plane-wave cutoff energy of

600 eV.

For formation enthalpy calculations of the pyrochlore, defect-fluorite, and weberite phases, larger supercells were constructed to ensure a reliable description of configurational disorder and structural relaxation. Specifically, 88-atom supercells were adopted for the pyrochlore and defect-fluorite structures, while a 176-atom supercell was used for the weberite structure. The Brillouin zone was sampled using a 3 × 3 × 3 k-point mesh for the pyrochlore and defect-fluorite phases, whereas a 2 × 2 × 4 mesh was employed for the weberite phase. The defect-fluorite and weberite configurations were generated using the SQS method [49] to represent the cation disorder. All formation enthalpy calculations were performed with a plane-wave cutoff energy of 600 eV.

For AIMD calculations, the same plane wave energy cutoff of 600 eV was employed, along with an automated 1 × 1 × 1 k-point mesh with the origin at the Γ point. To ensure the accuracy of the calculations and to eliminate finite-size effects on the displacement energy, a 2 × 2 × 1 supercell of the weberite structure containing 176 atoms was employed for the AIMD simulations. The 176-atom supercell configuration enabled explicit incorporation of PKAs for precise modeling of threshold displacement energy recoil dynamics. This cell size has been demonstrated in prior first-principles studies to be sufficient for capturing the local atomic rearrangements and defect formation processes [19,50,51]. Before initiating the PKA, these calculations employed the isothermal-isobaric (NPT) ensemble with triaxial periodic boundary constraints. The supercells were first equilibrated at 300 K over 3000 time steps, corresponding to a total simulation time of 300fs to ensure a stable thermal state. To simulate recoil events near the displacement threshold energy, the system was switched to the NVE ensemble with periodic boundary conditions in all directions. Individual atoms, including Gd (4b and 8 g), Lu (4b and 8 g), Zr (4a and 8 g), and O (16 h, 4c1, 4c2, and 4c3) (detailed in Section 2 and Fig. 1), were selected as PKAs, respectively. Recoil energies were imparted to each PKA along three primary crystallographic directions, namely ⟨100⟩, ⟨110⟩ and ⟨111⟩, as shown in Fig. 8. The trajectories of displaced atom were monitored for 2 ps [38]. If no stable defect formed within this timeframe, the recoil energy was incremented by 5 eV, and additional simulations were conducted. If the PKA failed to return to its original position, further simulations were performed with 1 eV precision to refine the displacement energy values. In these works, the ballistic phase, defect production, and stabilization typically occur within the first 1–1.5 ps, and extending the simulation time beyond 2 ps leads to negligible changes in the final defect configurations. Therefore, the present simulation setup is expected to capture the essential physics of the PKA process while ensuring computational efficiency. In addition, the three crystallographic directions we chose ⟨100⟩, ⟨110⟩, and ⟨111⟩ correspond to the main crystal axis of the weberite structure and can effectively represent the different local atomic environments around cations and anions. This approach follows previous first-principles studies of PKAs in complex oxide materials [37], where sampling along a limited set of high-symmetry directions was found sufficient to capture the main anisotropic features of displacement energies. Although a more extensive directional sampling would offer better statistical averaging, it is computationally prohibitive for AIMD simulations of systems of this size and complexity. Therefore, the selected directions provide a reasonable balance between computational cost and representativeness of the PKA behavior. Dynamics visualizations were generated using VESTA [52] and OVTIO [53], enabling detailed analysis of defect structures and atomic trajectories.

3. Results

3.1. Structural and electronic properties of $A_2Zr_2O_7$ (A = Gd, Lu) weberites

The atomic positions in $Gd_2Zr_2O_7$ weberite and $Lu_2Zr_2O_7$ weberite remain largely unchanged after 6000 structural equilibration steps at 300 K, as confirmed by AIMD simulations (Fig. 2). Throughout the entire simulation, only small thermal fluctuations around the equilibrium sites are observed, and the system energy exhibits no significant oscillations, indicating good structural stability. These findings are consistent with our previous theoretical results as well as experimental observations [50], further confirming the stability of $Gd_2Zr_2O_7$ weberite and $Lu_2Zr_2O_7$ weberite at 300 K. Moreover, the calculated formation enthalpies of the pyrochlore, defect-fluorite, and weberite phases provide additional support for their structural stability, as detailed in Section 4.1.

The optimized lattice constants and bond lengths of the $Gd_2Zr_2O_7$ weberite and $Lu_2Zr_2O_7$ weberite are summarized in Table 1. For $Gd_2Zr_2O_7$ weberite, the lattice constants of the orthorhombic unit cell are a = 10.50 Å, b = 7.42 Å, and c = 7.41 Å. The bond length of ⟨Gd-O⟩ ranges from 2.258 Å to 2.721 Å, while the ⟨Zr-O⟩ bond length varies between 2.054 Å and 2.437 Å. For $Lu_2Zr_2O_7$ weberite, the lattice constants of the orthorhombic unit cell are a = 10.32 Å, b = 7.33 Å, and c = 7.27 Å. The bond length of ⟨Lu-O⟩ ranges from 2.203 Å to 2.623 Å, while the ⟨Zr-O⟩ bond length varies between 2.063 Å and 2.358 Å. Notably, bond lengths of the same type exhibit slight variations across the crystal structure, the distorted configurations of ⟨Lu-O⟩ and ⟨Zr-O⟩ coordination polyhedra suggest significant geometric irregularity. A comparative analysis of the structural properties of $Gd_2Zr_2O_7$ weberite and $Lu_2Zr_2O_7$ weberite reveals that the lattice constant of $Gd_2Zr_2O_7$ [50] is larger than that of $Lu_2Zr_2O_7$. When the A-site cation changes from Gd to Lu, both the ⟨A-O⟩ and ⟨Zr-O⟩ bond lengths generally decrease, accompanied by an increase in bond strength. This observation aligns with the established trend that the relative stability of $A_2Zr_2O_7$ (A = Gd, Lu) weberites increases with the decreasing ionic radius of the A^{3+} cation [17].

In our calculations, the Gd 4f and Lu 4f electrons were treated as core states. To investigate the influence of 4f-electron treatment on the electronic properties of $Gd_2Zr_2O_7$ and $Lu_2Zr_2O_7$ weberite structures, we systematically compared three computational approaches: (a) treating the 4f electrons as core states in DFT (DFT-f core), (b) treating the 4f electrons as valence states in DFT (DFT-f valence), and (c) applying the DFT+U method with 4f electrons as valence states (DFT+U-f valence). This comparative framework for evaluating 4f-electron treatments had previously been employed in studies of $A_2Zr_2O_7$ (A = Nd, Sm, Gd, Yb) pyrochlores [45,46]. The valence configurations are $4f^7 5s^2 5p^6 5d^1 6s^2$ for Gd and $4f^{14} 5p^6 5d^1 6s^1$ for Lu. A Hubbard U correction of 4 eV was applied to the Gd 4f electrons [54]. For Lu 4f electrons, U_{eff} = 4.4 eV was employed [55].

The density of states (DOS) provides insights into the electronic structure by reflecting the distribution of electrons across different orbitals. Fig. 3 shows a comparison of the total density of states (TDOS) and partial density of states (PDOS) for $Gd_2Zr_2O_7$ and $Lu_2Zr_2O_7$ weberites under three different 4f-electron treatment methods. In the case of $Gd_2Zr_2O_7$ weberite, the valence band maximum (VBM) is primarily determined by the O 2p states near the Fermi level and the conduction band minimum (CBM) arises from the Gd 5d and Zr 4d orbitals. Notably, the hybridization between Gd 5d and O 2p orbitals is comparable to that between Zr 4d and O 2p orbitals. Similarly, for $Lu_2Zr_2O_7$ weberite, the VBM is primarily contributed by O 2p states, while the CBM is influenced by the Lu 5d and Zr 4d orbitals. Additionally, the hybridization between Lu 5d and O 2p orbitals closely resembles that of Zr 4d and O 2p orbitals.

When Gd/Lu 4f electrons are treated as core states, the VBM is primarily contributed by O 2p orbitals hybridized with Zr 4d and Gd 5d orbitals. In contrast, when Gd/Lu 4f electrons are treated as valence states without Hubbard U correction, the Gd 4f orbitals significantly contribute to the VBM and hybridize with O 2p and Zr 4d states. The CBM is also dominated by Gd 4f orbitals. This occurs because the Gd 4f states reside 1.64 eV above the Fermi level (Fig. 3 (a)), while Lu-4f states lie at 2.46 eV (Fig. 3 (b)). In DFT-f valence, the absence of strong correlation corrections leads to excessive delocalization of 4f electrons,

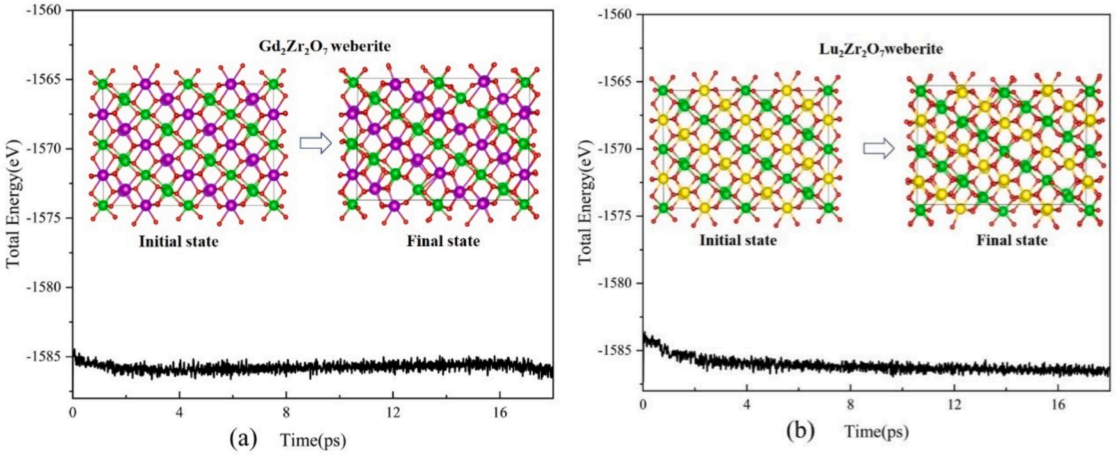

Fig. 2. Time-dependent total energy trajectories spanning the initial-to-final state transition for (a) $Gd_2Zr_2O_7$ weberite and (b) $Lu_2Zr_2O_7$ weberite.

Table 1
The lattice constant and bond length of $Gd_2Zr_2O_7$ weberite and $Lu_2Zr_2O_7$ weberite.

$Gd_2Zr_2O_7$ weberite		$Lu_2Zr_2O_7$ weberite	
Lattice constant [50]	a=10.50Å, b=7.42Å, c=7.41Å	Lattice constant	a=10.32Å, b=7.33Å, c=7.27Å
Lattice volume	$0.58nm^3$	Lattice volume	$0.55nm^3$
<Gd_{4b}-O_{4c}>	2.346Å-2.367Å	<Lu_{4b}-O_{4c}>	2.293Å-2.310Å
<Gd_{4b}-O_{16h}>	2.402Å-2.721Å	<Lu_{4b}-O_{16h}>	2.371Å-2.623Å
<Gd_{8g}-O_{16h}>	2.299Å-2.377Å	<Lu_{8g}-O_{16h}>	2.212Å-2.346Å
<Gd_{8g}-O_{4c}>	2.258Å-2.403Å	<Lu_{8g}-O_{4c}>	2.203Å-2.293Å
<Zr_{4a}-O_{16h}>	2.075Å-2.078Å	<Zr_{4a}-O_{16h}>	2.063Å-2.075Å
<Zr_{4a}-O_{4c}>	2.089Å	<Zr_{4a}-O_{4c}>	2.066Å
<Zr_{8g}-O_{16h}>	2.079Å-2.437Å	<Zr_{8g}-O_{16h}>	2.083Å-2.358Å
<Zr_{8g}-O_{4c}>	2.054Å-2.187Å	<Zr_{8g}-O_{4c}>	2.144Å-2.152Å

potentially causing physical distortions in the electronic structure description [45]. For DFT+U-f valence, Fermi level (Fig. 3 (a)), far from the O 2p-dominated VBM and Zr 4d-dominated CBM. The contracted 4f orbitals, strongly shielded by 5d/6 s orbitals, exhibit high localization due to suppressed orbital interactions between Gd and ligands [45,56]. Despite these differences, the band gaps of $Gd_2Zr_2O_7$ weberite are similar: the Gd-4f states are shifted to 4.50 eV above the 3.12 eV (DFT-f core), 3.38 eV (DFT-f valence), and 3.36 eV (DFT+U-f valence) (Fig. 3 (a)). Similarly, $Lu_2Zr_2O_7$ weberite exhibits comparable values: 3.17 eV, 3.22 eV, and 3.04 eV (Fig. 3 (b)). This confirms U-value independence, validating the safe treatment of 4f orbitals as core states, consistent with pyrochlore studies [19,45–47,54,56,57].

To better resolve the differences in the conduction band (CB) region between $Gd_2Zr_2O_7$ and $Lu_2Zr_2O_7$ weberites, Fig. 4 presents the total and partial DOS over a narrower energy range (-5 eV to 10 eV). While the nominal valence electronic configurations of Gd and Lu are identical ($5p^6 5d^1 6s^2$), the CB profiles differ markedly due to the lanthanide contraction effect. The smaller ionic radius of Lu^{3+} shortens the ⟨Lu-O⟩ bond length, enhancing crystal field splitting and modifying the hybridization strength between Lu 5d and O 2p orbitals. This results in a slight upward shift and redistribution of Lu 5d states in the CB region, compared to the Gd 5d states in $Gd_2Zr_2O_7$. In addition, the hybridization between A-cation d orbitals and O 2p states is stronger in $Lu_2Zr_2O_7$, leading to a broader CB onset and a reduced DOS peak intensity near the CBM. These differences are consistent with the observed variations in bonding characteristics and local lattice distortions, which subsequently

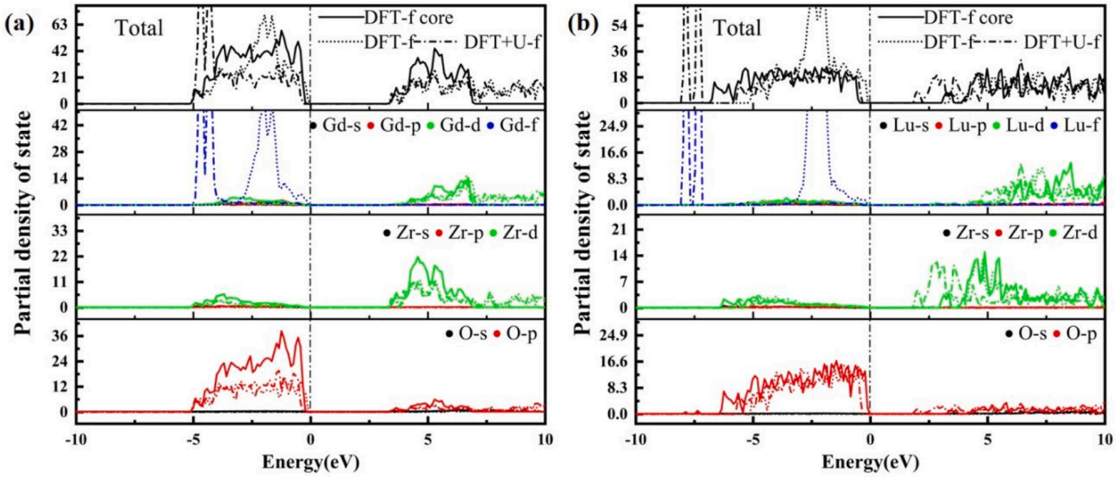

Fig. 3. Presents a comparison of the total density of states (TDOS) and partial density of states (PDOS) for (a) $Gd_2Zr_2O_7$ and (b) $Lu_2Zr_2O_7$ weberites under three different 4f-electron treatment methods: treating the 4f electrons as core states in DFT (DFT-f core), represented by solid lines; treating the 4f electrons as valence states in DFT (DFT-f valence), depicted with dotted lines; applying the DFT+U method with 4f electrons treated as valence states (DFT+U-f valence), indicated by short dot underline, where U_{eff} = 4 eV for Gd 4f and U_{eff} = 4.4 eV for Lu 4f.

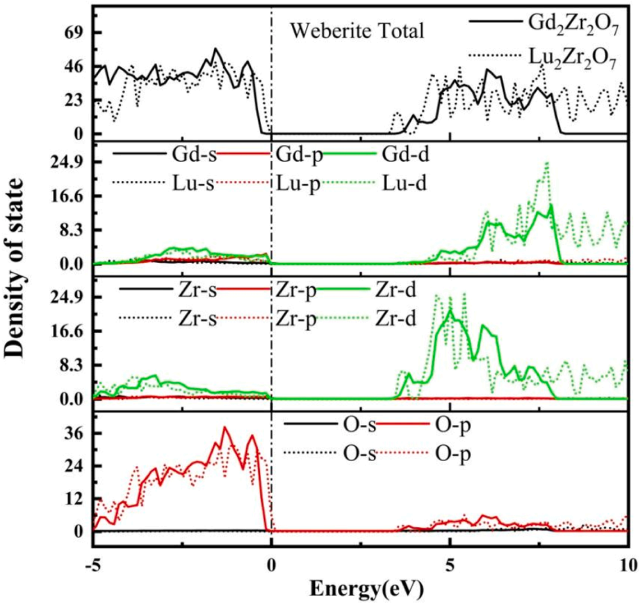

Fig. 4. Comparison of TDOS and PDOS for $Gd_2Zr_2O_7$ and $Lu_2Zr_2O_7$ weberites in the energy range of -5 eV to 10 eV, the TDOS and PDOS of $Gd_2Zr_2O_7$ weberite are represented by solid lines, and the TDOS and PDOS of $Lu_2Zr_2O_7$ weberite are represented by dotted lines.

influence defect energetics and irradiation resistance, as discussed in Section 4.4.

3.2. Influence of He doping at different interstitial sites on the structural and electronic properties of $A_2Zr_2O_7$ (A = Gd, Lu) weberites

To investigate the effect of a single He interstitial on $A_2Zr_2O_7$ (A = Gd, Lu) weberites, twelve distinct He interstitial sites were considered within the 44 atoms lattice unit. The configurations of these He interstitials are illustrated in Figs. 5 (a)-(l), using He-$Gd_2Zr_2O_7$ weberites as a reference. A complete structural relaxation of He-$A_2Zr_2O_7$ (A = Gd, Lu) weberites was carried out, and the corresponding volumes and lattice constants are presented in Table 2.

Table 2 provides the effects of He doping on volume and lattice constant changes along three crystallographic directions for both weberite systems. The introduction of He interstitials led to lattice expansion in both structures. Specifically, the volume of $Gd_2Zr_2O_7$ weberite increased by 3.48% (He at the Gd-Gd interstitial site), 2.85% (He at the Zr-Zr interstitial site), 2.86% (He at the O—O interstitial site), and 2.91% (He at the octahedral interstitial site). In contrast, $Lu_2Zr_2O_7$ weberite exhibites slightly lower volume increases: 3.15% (He at the Lu-Lu interstitial site), 2.42% (He at the Zr-Zr interstitial site), 2.73% (He at the O—O interstitial site), and 2.36% (He at the octahedral interstitial site). These results indicate that the incorporation of He leads to structural distortion. In the He-$A_2Zr_2O_7$ (A = Gd, Lu) weberites, except for He-doped A_{8g}-A_{8g} interstitial sites, the He interstitials at other positions tend to relax and migrate toward the octahedral sites.

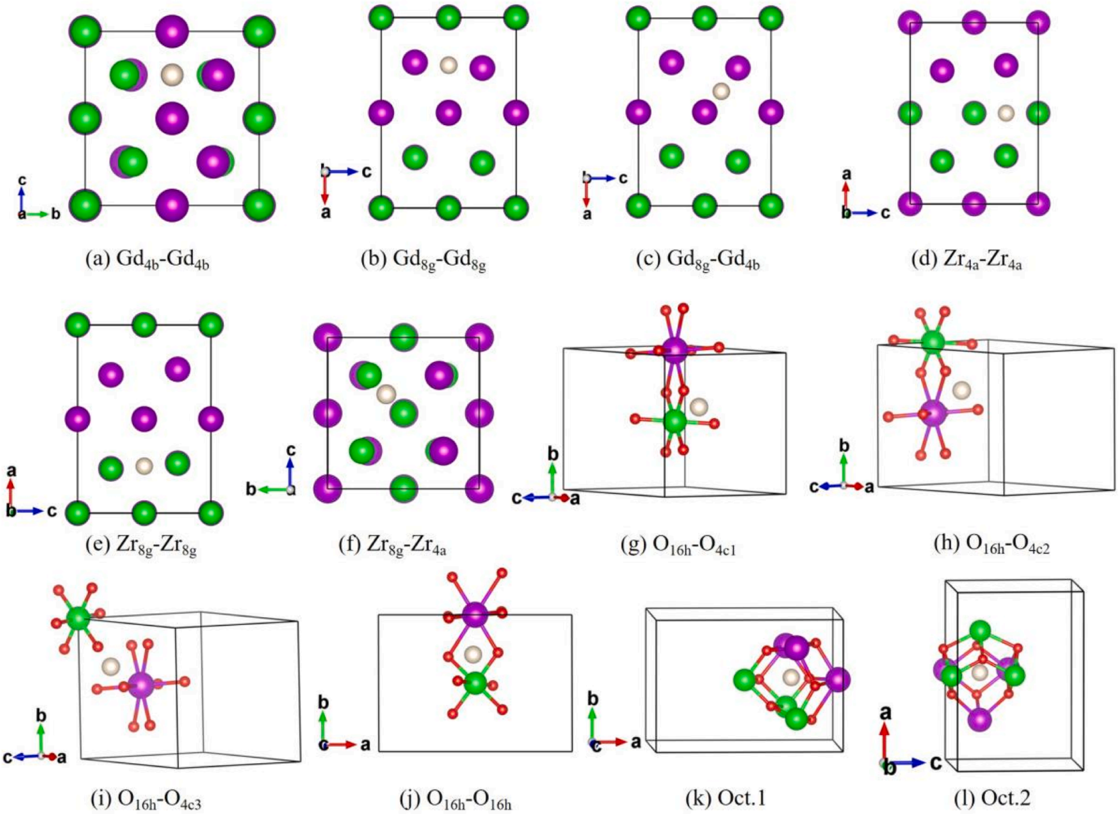

(a) Gd_{4b}-Gd_{4b}
(b) Gd_{8g}-Gd_{8g}
(c) Gd_{8g}-Gd_{4b}
(d) Zr_{4a}-Zr_{4a}
(e) Zr_{8g}-Zr_{8g}
(f) Zr_{8g}-Zr_{4a}
(g) O_{16h}-O_{4c1}
(h) O_{16h}-O_{4c2}
(i) O_{16h}-O_{4c3}
(j) O_{16h}-O_{16h}
(k) Oct.1
(l) Oct.2

Fig. 5. Configurations of different interstitial positions of He in $Gd_2Zr_2O_7$ weberite. (a) He interstitial located at the middle between two gadolinium atoms at 4b position; (b) He interstitial located at the middle of two gadolinium atoms at 8 g position; (c) He interstitial located at the middle of one gadolinium atom at the 8 g position and one gadolinium atom at the 4b position; (d) He interstitial located at the middle between two zirconium atoms at 4a position; (e) He interstitial located at the middle between two zirconium atoms at 8 g position; (f) He interstitial located at the middle of one zirconium atom at the 8 g position and one zirconium atom at the 4a position; (g) He interstitial located at the middle of one oxygen atom at the 16 h position and one oxygen atom at the 4c1 position; (h) He interstitial located at the middle of one oxygen atom at the 16 h position and one oxygen atom at the 4c2 position; (i) He interstitial located at the middle of one oxygen atom at the 16 h position and one oxygen atom at the 4c3 position; (j) He interstitial located at the middle between two oxygen atoms at 16 h position; (k) He at the first octahedral position; (k) He at the second octahedral position. The white, purple, green and red spheres represent He, Gd, Zr and O, respectively.

Table 2
Results of the volume (nm^3), lattice constant a (Å), b (Å), c (Å).

			V (nm^3)	a (Å)	b (Å)	c (Å)
$Gd_2Zr_2O_7$ weberite			0.585	10.500	7.427	7.416
He-$Gd_2Zr_2O_7$	Gd-Gd	Gd_{4b}-Gd_{4b}	0.602	10.616	7.554	7.508
		Gd_{8g}-Gd_{8g}	0.612	10.696	7.498	7.638
		Gd_{8g}-Gd_{4b}	0.602	10.606	7.564	7.505
	Zr-Zr	Zr_{4a}-Zr_{4a}	0.600	10.599	7.543	7.504
		Zr_{8g}-Zr_{8g}	0.604	10.657	7.437	7.627
		Zr_{8g}-Zr_{4a}	0.601	10.592	7.511	7.561
	O-O	O_{16h}-O_{4c1}	0.602	10.590	7.521	7.557
		O_{16h}-O_{4c2}	0.601	10.587	7.508	7.568
		O_{16h}-O_{4c3}	0.602	10.608	7.548	7.513
		O_{16h}-O_{16h}	0.602	10.592	7.511	7.570
	Oct.	Oct.1	0.603	10.600	7.547	7.538
		Oct.2	0.601	10.606	7.544	7.505
$Lu_2Zr_2O_7$ weberite			0.550	10.316	7.329	7.271
He-$Lu_2Zr_2O_7$	Lu-Lu	Lu_{4b}-Lu_{4b}	0.565	10.390	7.444	7.300
		Lu_{8g}-Lu_{8g}	0.571	10.452	7.379	7.411
		Lu_{8g}-Lu_{4b}	0.566	10.392	7.443	7.311
	Zr-Zr	Zr_{4a}-Zr_{4a}	0.563	10.386	7.420	7.310
		Zr_{8g}-Zr_{8g}	0.564	10.437	7.260	7.442
		Zr_{8g}-Zr_{4a}	0.563	10.386	7.411	7.313
	O-O	O_{16h}-O_{4c1}	0.565	10.394	7.376	7.372
		O_{16h}-O_{4c2}	0.563	10.382	7.367	7.363
		O_{16h}-O_{4c3}	0.565	10.382	7.430	7.328
		O_{16h}-O_{16h}	0.567	10.397	7.434	7.332
	Oct.	Oct.1	0.563	10.381	7.427	7.304
		Oct.2	0.563	10.390	7.416	7.307

The electronic structure of a material significantly influences its physical and structural properties [58,59]. To further understand the relative stability of the He-doped $A_2Zr_2O_7$ (A = Gd, Lu) weberites, the PDOS and Bader charge [60–63] were calculated to analyze the effects of He interstitials on the electronic structure of $A_2Zr_2O_7$ (A = Gd, Lu) weberites. The difference in PDOS between the He-doped and pure $A_2Zr_2O_7$ (A = Gd, Lu) weberite systems was calculated using the following formula:

$$\Delta PDOS = PDOS_{He-A_2Zr_2O_7} - PDOS_{A_2Zr_2O_7}.$$

ΔPDOS directly reflects bonding strength changes by comparing orbital-projected density of states before and after doping, where zero, positive, and negative values correspond to unchanged, increased, and decreased PDOS, respectively, in He-doped versus pure $A_2Zr_2O_7$ (A = Gd, Lu) weberites. For $Gd_2Zr_2O_7$ weberite, notably negative ΔPDOS values occur at Gd 5d and O 2p orbitals, while smaller negative shifts appear at Zr 4d orbitals (Fig. S1). This indicates weakened covalency in both ⟨Gd-O⟩ and ⟨Zr-O⟩ bonds, consistent with Bader charge analyses in Section 4.2. In $Lu_2Zr_2O_7$ weberite, significant negative ΔPDOS values are observed for O 2p orbitals, while minimal changes occur at Lu 5d and subtle negative shifts appear at Zr 4d orbitals (Fig. S2), suggesting stable ⟨Lu-O⟩ bonds with slightly weakened ⟨Zr-O⟩ covalency. Bader charge analyses further confirm stronger covalency in ⟨Lu-O⟩ bonds versus weaker ⟨Zr-O⟩ interactions. ΔPDOS is typically combined with Bader charges and defect formation energies to comprehensively evaluate amorphization resistance [64], as weaker covalent networks dissipate radiation energy more effectively, mitigating damage accumulation [30,65]. A deeper assessment of weberites irradiation resistance is provided in Section 4.2.

3.3. Preferable location of He in $A_2Zr_2O_7$ (A = Gd, Lu) weberites

The formation energy frequently serves as a key parameter for assessing the relative stability of interstitial atoms within compounds [25,65–70], lower values indicate He is more likely to occupy the site under thermal equilibrium, potentially increasing local lattice strain and affecting radiation damage evolution, indicating higher structural stability. The formation energy of He interstitials in $A_2Zr_2O_7$ (A = Gd, Lu) weberites was calculated using the following equation [67]:

$$E_f^{He(Int)} = E_{He-A_2Zr_2O_7} - E_{A_2Zr_2O_7} - E_{He}$$

Where $E_{He-A_2Zr_2O_7}$ is the total energy of the $A_2Zr_2O_7$ (A = Gd, Lu) weberite system with He interstitials. $E_{A_2Zr_2O_7}$ is the total energy of the pure $A_2Zr_2O_7$ (A = Gd, Lu) weberite system, and E_{He} corresponds to the ground state energy pertaining to an isolated He atomic system. For He atoms occupying pre-existing vacancies, the formation energy is calculated as [67]:

$$E_f^{He(Vac)} = E_{He+Vac} - E_{Vac} - E_{He}$$

Where E_{He+Vac} is the total energy of the $A_2Zr_2O_7$ (A = Gd, Lu) weberite system with He atoms occupying vacancies. E_{Vac} represents the total energy of the $A_2Zr_2O_7$ (A = Gd, Lu) weberite system with vacancy defects, and E_{He} corresponds to the ground state energy pertaining to an isolated He atomic system.

Formation energy results are presented in Table 3 and Fig. 10. Among all interstitial sites, the A_{8g}-A_{8g} sites are the most unstable interstitial sites for He to occupy, as they exhibit the highest formation energies of 3.353 eV and 3.676 eV, respectively. This correlates with the largest volume changes observed in Table 2. In contrast, for most other interstitial sites, the formation energies are relatively low. Specifically, in the He-$Gd_2Zr_2O_7$ weberite, the formation energy for He at interstitial sites (excluding A8g-A8g) averages around 1.278 eV, while in the He-$Lu_2Zr_2O_7$ weberite, it is approximately 2.220 eV. Notably, He interstitials at most positions tend to migrate toward octahedral sites upon relaxation, except for the A_{8g}-A_{8g} interstitial site. This behavior indicates a preference for He atoms to occupy the octahedral interstitial sites, which aligns with observations in pyrochlore [64].

Regarding He incorporation into vacancy sites, the results indicate that in the $Gd_2Zr_2O_7$ weberite, the O_{4c3} (1.194 eV) and O_{16h} (1.263 eV) vacancies are the most favorable sites for He atoms, whereas the Zr_{8g} vacancy (2.9 eV) is the least stable. In $Lu_2Zr_2O_7$ weberite, the Lu_{4b} (1.331 eV) and Lu_{8g} (1.361 eV) vacancies are preferred, while the O_{4c1} vacancy exhibits the highest formation energy (3.488 eV), making it the least favorable site for He incorporation.

3.4. Binding energy

The accumulation of He atoms in a material increases its He concentration, which can significantly impact the crystallographic structure and chemical stability of the matrix [71]. To investigate the effects of He clusters, two He atoms were introduced into 12 different interstitial sites in $A_2Zr_2O_7$ (A = Gd, Lu) weberites, corresponding to a concentration of 2.2 at.%. The binding energies of He atoms in these interstitial positions were systematically calculated, and the corresponding results are summarized in Table 4.

Binding energy is widely used to assess the stability of defect cluster [72,73] in a material. The binding energy of two He atoms at various interstitial sites in the $A_2Zr_2O_7$ (A = Gd, Lu) weberites are calculated using the following formula [74]:

$$E_b^{2He} = E_{bulk+2He} + E_{bulk} - 2E_{bulk+He}$$

Table 3

Formation energies of He atoms at different interstitial positions ($E_f^{He(Int)}$) and pre-existing vacancy positions ($E_f^{He(Vac)}$) .

Formation energy(eV)	$E_f^{He(Int)}$											
Site	A_{4b}-A_{4b}	A_{8g}-A_{8g}	A_{8g}-A_{4b}	Zr_{4a}-Zr_{4a}	Zr_{8g}-Zr_{8g}	Zr_{8g}-Zr_{4a}	O_{16h}-O_{4c1}	O_{16h}-O_{4c2}	O_{16h}-O_{4c3}	O_{16h}-O_{16h}	Oct.1	Oct.2
$Gd_2Zr_2O_7$	1.311	3.353	1.261	1.469	1.200	1.160	1.180	1.155	1.310	1.158	1.382	1.471
$Lu_2Zr_2O_7$	2.217	3.676	2.353	2.375	2.014	2.394	2.073	2.044	2.242	2.206	2.233	2.270

Formation energy(eV)	$E_f^{He(Vac)}$							
Vacancy	A_{4b}	A_{8g}	Zr_{4a}	Zr_{8g}	O_{16h}	O_{4c1}	O_{4c2}	O_{4c3}
$Gd_2Zr_2O_7$	1.664	1.683	2.644	2.900	1.263	2.576	1.997	1.194
$Lu_2Zr_2O_7$	1.331	1.361	1.923	1.493	2.151	3.488	2.478	2.199

Table 4

Binding energies of two He atoms incorporated into $A_2Zr_2O_7$ (A = Gd, Lu) weberites.

Configuration		Binding energy (eV)	Configuration		Binding energy (eV)
He-$Gd_2Zr_2O_7$ weberite	Gd_{4b}-Gd_{4b}	0.934	He-$Lu_2Zr_2O_7$ weberite	Lu_{4b}-Lu_{4b}	-0.186
	Gd_{8g}-Gd_{8g}	-4.252		Lu_{8g}-Lu_{8g}	-3.967
	Gd_{8g}-Gd_{4b}	-0.170		Lu_{8g}-Lu_{4b}	-1.120
	Zr_{4a}-Zr_{4a}	-0.211		Zr_{4a}-Zr_{4a}	-0.999
	Zr_{8g}-Zr_{8g}	-0.155		Zr_{8g}-Zr_{8g}	1.167
	Zr_{8g}-Zr_{4a}	-0.171		Zr_{8g}-Zr_{4a}	-1.249
	O_{16h}-O_{4c1}	0.039		O_{16h}-O_{4c1}	-0.834
	O_{16h}-O_{4c2}	0.109		O_{16h}-O_{4c2}	-0.724
	O_{16h}-O_{4c3}	-0.440		O_{16h}-O_{4c3}	-1.295
	O_{16h}-O_{16h}	-0.114		O_{16h}-O_{16h}	-0.984
	Oct.1	-0.345		Oct.1	-0.346
	Oct.2	-0.206		Oct.2	-1.025

Here, $E_{bulk+2He}$ is the total energy of the $A_2Zr_2O_7$ (A = Gd, Lu) weberite system with two He atoms at interstitial sites, while $E_{bulk+He}$ represents the total energy of the $A_2Zr_2O_7$ (A = Gd, Lu) weberite system with one He atom at interstitial sites. E_{bulk} is the total energy of the pure $A_2Zr_2O_7$ (A = Gd, Lu) weberite system.

The calculated binding energies are listed in Table 4. A negative binding energy indicates that He atoms tend to form stable clusters at these sites, whereas a positive binding energy suggests that clustering at the given interstitial positions is energetically unfavorable [72]. In the $Gd_2Zr_2O_7$ weberite, the binding energies at the Gd_{4b}-Gd_{4b}, O_{16h}-O_{4c1}, and O_{16h}-O_{4c2} positions are positive, with values of 0.934 eV, 0.039 eV, and 0.109 eV, respectively. This indicates that He clustering at these sites is less favorable. However, at all other interstitial sites, the binding energies are negative, indicating that He clustering is energetically preferred. Similarly, in the $Lu_2Zr_2O_7$ weberite, the Zr_{8g}-Zr_{8g} interstitial site exhibits a positive binding energy of 1.167 eV, implying that He clustering at this site is unlikely. Conversely, all other interstitial sites show negative binding energies, indicating a preference for He clustering. To assess the influence of dispersion interactions, the binding energy of the He-$Gd_2Zr_2O_7$ system containing two He atoms was recalculated with dispersion correction as a representative example. As shown in the Supplementary Information (Fig. S3), the inclusion of dispersion correction does not significantly affect the qualitative trends or conclusions of this work.

3.5. Cation antisite defect formation energy

To assess the impact of He incorporation on the radiation tolerance of $A_2Zr_2O_7$ (A = Gd, Lu) weberites, we calculated the formation energies of cation antisite defects, as shown in Fig. 7 (a)-(b). Cation antisite defects arise from the exchange of two neighboring cations within the weberite framework [75]. Using the $Gd_2Zr_2O_7$ weberite as an example, various antisite defect configurations within the cation sublattice were considered, as illustrated in Fig. 6. The formation energy of these defects is computed using the following formula [64]:

$$E_f^{CA} = E_{tot}^{CA} - E_{tot}$$

where E_{tot}^{CA} is the total energy of the $A_2Zr_2O_7$ (A = Gd, Lu) weberite system or the He-doped $A_2Zr_2O_7$ (A = Gd, Lu) weberite system with a cation antisite defect, and E_{tot} is the total energy of the defect-free system.

In the $Gd_2Zr_2O_7$ weberite, the highest formation energy of cation antisite defects is 1.78 eV, which is lower than the 2.08 eV observed in $Gd_2Zr_2O_7$ pyrochlore [50,54]. These findings demonstrate that cation antisite defects exhibit a greater tendency to form in weberite structures relative to pyrochlore configurations. As illustrated in Fig. 7 (a), among the cation antisite defects in $Gd_2Zr_2O_7$ weberite, the exchange between Gd (8 g) and Zr (8 g) sites exhibits the highest thermodynamic stability, whereas the Gd (4b)-Zr (4a) configuration demonstrates the lowest stability. The lowest formation energy occurs for the exchange of Gd (8 g) and Zr (8 g) cations along the (100) plane [50]. Upon He incorporation, the formation energies of cation antisite defects in He-$A_2Zr_2O_7$ (A = Gd, Lu) weberites generally decreases, and the most favorable cation antisite defect configurations are also altered with He doping. In the He-$Gd_2Zr_2O_7$ weberite, for the case of He located at the Gd_{4b}-Gd_{4b}, O_{16h}-O_{4c3}, Gd_{8g}-Gd_{4b}, and Zr_{4a}-Zr_{4a} interstitial sites, the most readily formed cation antisite defect configuration is the exchange configuration of Gd (4b) and Zr (4a) cations. For the case of He located at the Gd_{4b}-Gd_{4b} and O_{16h}-O_{4c3} interstitial sites, Gd (4b)-Zr (4a) cation antisite defects on the (100) plane is favorable to form. For the case of He located at the Zr_{8g}-Zr_{8g} interstitial sites, the cation antisite defect configuration involving the exchange of Gd(4b) and Zr(8 g) cations are more readily to form. For the other seven configurations in the He-$Gd_2Zr_2O_7$ weberite, the most easily formed cation antisite defect configurations involve the exchange of Gd (8 g) and Zr (8 g) cations, similar to that of the ideal $Gd_2Zr_2O_7$ weberite [50].

As shown in Fig. 7 (b), in the pure $Lu_2Zr_2O_7$ weberite, the most readily formed cation antisite defect configuration is Lu (8 g)-Zr (8 g) cation antisite defect, which is formed by the exchange of Lu (8 g) and Zr (8 g) cations, while the Lu (4b)-Zr (4a) cation antisite defect is the least favorable. The formation energy for the cation antisite defect resulting from the exchange of Lu (8 g) and Zr (8 g) cations on the (100) plane is 0.88 eV, which is higher than the minimum defect formation energy of 0.19 eV observed in the pure $Gd_2Zr_2O_7$ weberite. In the He-doped $Lu_2Zr_2O_7$ weberite, the most favorable cation antisite defect configuration depends on the He interstitial position. When He occupies the Zr_{8g}-

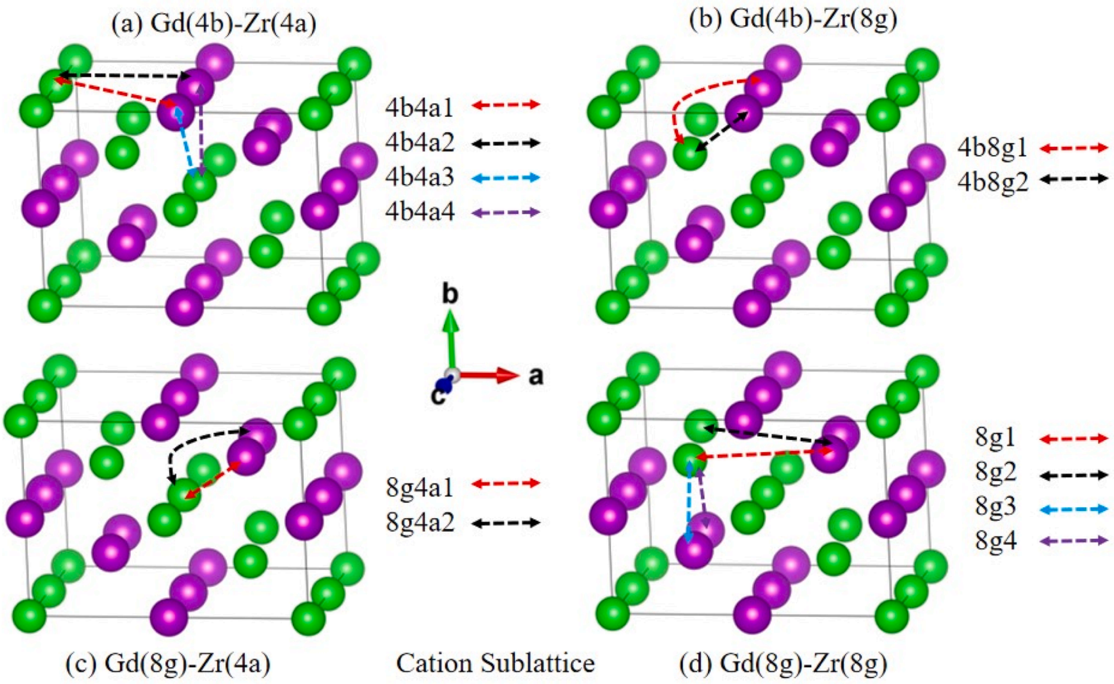

Fig. 6. Cation antisite defect configurations within the sublattice framework. (a)-(d) Illustrate Gd/Zr exchange processes at specific Wyckoff sites: (a) Gd (4b)-Zr (4a), (b) Gd (4b)-Zr (8 g), (c) Gd (8 g)-Zr (4a) and (d) Gd (8 g)-Zr (8 g), cation along the directions indicated by arrows.

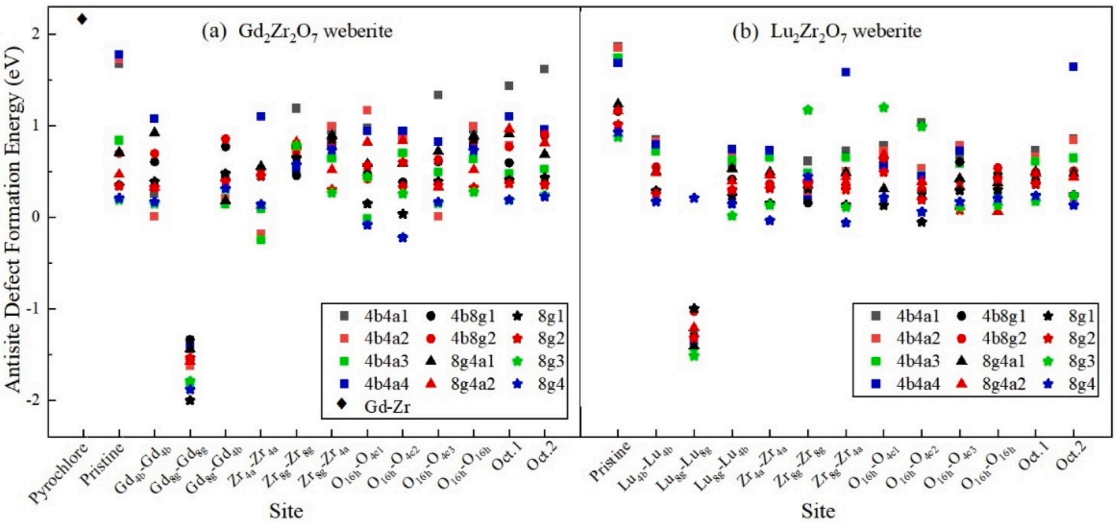

Fig. 7. The cation antisite defect formation energies of different configurations in $A_2Zr_2O_7$ (A= Gd, Lu) weberites, the configuration of different gap positions of He in weberite is shown in Fig. 5, the graph represents cation antisite defect configurations, such as square is A (4b)-Zr (4a), round is A (4b)-Zr (8 g), triangular is A (8 g)-Zr (4a), flower is A (8 g)-Zr (8 g), and diamond is pyrochlore's A-Zr: (a) $Gd_2Zr_2O_7$ weberite, compared with that of $Gd_2Zr_2O_7$ pyrochlore system [50], (b) $Lu_2Zr_2O_7$ weberite.

Zr_{8g} interstitial site, the Lu (4b)-Zr (8 g) cation antisite defect the atom becomes the most stable. When He is located at the O_{16h}-O_{16h} interstitial site, the Lu (8 g)-Zr (4a) cation antisite defect is the most energetically preferred configuration. In the other ten configurations, the predominant defect is the Lu (8 g)-Zr (8 g) cation antisite defect, consistent with the undoped $Lu_2Zr_2O_7$ weberite structure. Notably, when the He occupies the Lu_{8g}-Lu_{8g} interstitial site, the calculated negative defect formation energies indicate a higher likelihood of cation disorder in this configuration compared to others.

3.6. Displacement energies in $A_2Zr_2O_7$ (A = Gd, Lu) weberites

The threshold displacement energy is closely related to the radiation resistance of material [37,76]. In pyrochlore, a lower E_d facilitates the order-disorder phase transformation and enhancing ionic diffusion. These effects contribute to improved damage recovery and release stored energy, ultimately enhancing radiation resistance [77]. Tables 5 and 6 summarize the E_d for PKAs of Gd, Lu, Zr and O in $A_2Zr_2O_7$ (A = Gd, Lu) weberites along the principal crystallographic directions and the corresponding defect configurations.

The E_d exhibits anisotropy across the three principal crystallographic

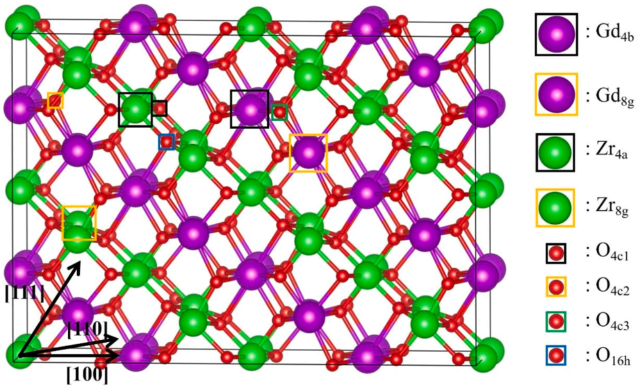

Fig. 8. Gd_{4b}, Gd_{8g}, Zr_{4a}, Zr_{8g}, O_{16h}, O_{4c1}, O_{4c2}, O_{4c3} as PKAs and representation of the main crystallographic directions in $Gd_2Zr_2O_7$ weberite systems. The purple, green, red and blue spheres represent Gd, Zr, O and intrinsic ordered vacancies, respectively.

directions in $A_2Zr_2O_7$ (A = Gd, Lu) weberites [37,51,76,77]. Among the cation PKAs, the Zr_{4a} recoils along the ⟨111⟩ direction have the lowest E_d, whereas other cation PKAs generally exhibit the lowest E_d along the ⟨100⟩ direction. In the case of A-site cation PKAs, the A_{4b} PKA along the ⟨100⟩ direction exhibits the lowest threshold displacement energy, with values of 11 eV in $Gd_2Zr_2O_7$ weberite and 16 eV in $Lu_2Zr_2O_7$ weberite. The defect configurations formed in both cases are remarkably similar. As the A_{4b} PKA moves along the predefined ⟨100⟩ direction, it displaces a neighboring Zr_{4a} atom, the displaced Zr_{4a} atom subsequently relaxed into the adjacent octahedral center site along the ⟨100⟩ direction under interatomic force mediation. For the B-site cation PKAs, the Zr_{4a} PKA in $Gd_2Zr_2O_7$ weberite exhibits the lowest E_d of 18 eV along the recoiling ⟨111⟩ direction. The Zr_{4a} PKA follows a prescribed trajectory along the ⟨111⟩ direction, colliding with a neighboring Zr_{4a} atom. The impacted Zr_{4a} relaxes back to its original position, forming an antisite cation defect involving the Zr_{4a} PKA. In $Lu_2Zr_2O_7$ weberite, the lowest E_d values are 30 eV for both Zr_{4a}[111] and Zr_{8g}[100]. The Zr_{4a} PKA travels a defined distance along the ⟨111⟩ direction, colliding with a neighboring Lu_{8g} atom, which is radially displaced from its lattice site. The displaced Lu_{8g} atom then relaxes back to its original position, while the Zr_{4a} PKA rests at an interstitial site, thereby forming a Frenkel defect pair. Meanwhile, the Zr_{8g} PKA moving along the ⟨100⟩ direction and interacts with a nearby Lu_{8g} atom, leading to a direct substitution of Lu_{8g} by Zr_{8g} and forcing the displaced Lu_{8g} into an interstitial site.

For oxygen PKAs, the lowest E_d in $Gd_2Zr_2O_7$ weberite is 1 eV for O_{16h}[111]. However, rather than moving strictly along ⟨111⟩, the O_{16h} PKA undergoes an interatomic interaction-driven displacement of 1.613 Å towards the ⟨011⟩ direction, ultimately ending in the intrinsic vacancy at a 4c site. In $Lu_2Zr_2O_7$ weberite, the O_{4c3}[100] has the lowest E_d value of 10 eV. The O_{4c3} PKA moves a certain distance along the ⟨100⟩ direction before colliding with an adjacent O_{4c1} atom. As a result, the O_{4c1} atom is displaced by 2.376 Å along the ⟨100⟩ direction and subsequently occupies the intrinsic vacancy at a 4c site. Our simulations show that, after such collision events, oxygen ions predominantly locate at the intrinsic vacancies at 4c sites.

Table 5
Threshold displacement energies and resulting defect structures for cation (A = Gd or Lu, B = Zr) recoils in $A_2Zr_2O_7$ (A = Gd, Lu) weberite. X_{vac}: vacancy of X-type atoms; X_Y: X interstitial occupying the Y site; X_{bri}: X interstitial at the bridge site; X_{4c}: X interstitial occupying a 4c site. In our work, X_{int} indicates X interstitial occupying an interstitial site, but not 4c, bridge or Y. E_d: threshold displacement energy.

$Gd_2Zr_2O_7$ weberite			$Lu_2Zr_2O_7$ weberite	
PKA	E_d(eV)	Defects	E_d(eV)	Defects
A_{4b}[100]	11	$Gd_{vac}+Gd_{Zr}+Zr_{int}+3O_{vac}+2O_{bri}+O_{4c}$	16	$Lu_{vac}+Lu_{Zr}+Zr_{int}+3O_{vac}+O_{4c}+O_{int}$
A_{4b}[110]	14	$Gd_{vac}+Gd_{int}2O_{vac}+O_{bri}+O_{4c}$	20	$2Lu_{vac}+2Lu_{int}+4O_{vac}+3O_{4C}+O_{int}$
A_{4b}[111]	35	$Gd_{vac}+Gd_{int}+Zr_{vac}+Zr_{int}+2O_{vac}+ 2O_{4c}$	31	$Lu_{vac}+Lu_{int}+Zr_{vac}+Zr_{int}+5O_{vac}+2O_{4c} +3O_{int}$
A_{8g}[100]	13	$Gd_{vac}+Gd_{int}+3O_{vac}+O_{bri}+2O_{4c}$	23	antisite defect (Lu_{8g} and Lu_{4b}) $+2O_{vac}+2O_{4c}$
A_{8g}[110]	15	antisite defect (Gd_{8g} and Zr_{4a}) $+O_{vac}+O_{4c}$	28	$2Lu_{vac}+2Lu_{int}+Zr_{vac}+Zr_{int}+5O_{vac}+3O_{4c}+2O_{int}$
A_{8g}[111]	25	$Gd_{vac}+Gd_{Zr}+Zr_{int}+7O_{vac}+2O_{bri}\ 4O_{4c}+O_{int}$	31	$Lu_{vac}+Lu_{Zr}+Zr_{int}+5O_{vac}+2O_{4c}+3O_{int}$
Zr_{4a}[100]	23	$Zr_{vac}+Zr_{int}+O_{vac}+O_{4c}$	33	$Zr_{vac}+2Lu_{vac}+Lu_{zr}+2Zr_{int}+Lu_{int}+4O_{vac}+4O_{4c}$
Zr_{4a}[110]	30	$Zr_{Gd}+Gd_{Gd}+Gd_{Zr}4O_{vac}+3O_{4c}+O_{int}$	41	$Zr_{Lu}+Zr_{Zr}+Lu_{Zr}+4O_{vac}+3O_{4c}+O_{int}$
Zr_{4a}[111]	18	antisite defect (Zr_{4a} and Zr_{4a}) $+3O_{vac}+O_{int}+2O_{4c}$	30	$Zr_{vac}+Zr_{int}+4O_{vac}+4O_{4c}$
Zr_{8g}[100]	25	$Zr_{vac}+Zr_{Gd}+Gd_{int}+3O_{vac}+3O_{4c}$	30	$Zr_{vac}+Zr_{Lu}+Lu_{int}+4O_{vac}+3O_{4c}+O_{int}$
Zr_{8g}[110]	29	antisite defect (Zr_{8g} and Gd_{4b}) $+2O_{vac}+ 2O_{4c}$	37	antisite defect (Zr_{8g} and Lu_{4b}) $+O_{vac}+O_{4c}$
Zr_{8g}[111]	31	antisite defect (Zr_{8g} and Zr_{8g}) $+6\ O_{vac}+ 6O_{4c}$	31	$Zr_{vac}+Zr_{Lu}+Lu_{int}+5O_{vac}+2O_{4c}+3O_{int}$

Table 6
Threshold displacement energies and resulting defect structures for oxygen recoils in $A_2Zr_2O_7$ (A = Gd, Lu) weberite. X_{vac}: vacancy of X-type atoms; X_Y: X interstitial occupying the Y site; X_{bri}: X interstitial at the bridge site; X_{4c}: X interstitial occupying a 4c site. X_{int} indicates X interstitial occupying an interstitial site, but not 4c, bridge or Y. E_d: threshold displacement energy.

$Gd_2Zr_2O_7$ weberite			$Lu_2Zr_2O_7$ weberite	
PKA	E_d(eV)	Defects	E_d(eV)	Defects
O_{4c1}[100]	21	$4O_{vac}+2O_{4c}+2O_{int}$	34	$6O_{vac}+5O_{4c}+O_{int}$
O_{4c1}[110]	35	$Gd_{vac}+Gd_{int}+3O_{vac}+2O_{4c}+2O_{int}$	36	$7O_{vac}+7O_{4c}$
O_{4c1}[111]	5	$O_{vac}+O_{4c}$	12	$2O_{vac}+2O_{4c}$
O_{4c2}[100]	9	$2O_{vac}+2O_{4c}$	16	$3O_{vac}+2O_{4c}+O_{int}$
O_{4c2}[110]	10	$O_{vac}+O_{4c}$	13	$3O_{vac}+3O_{4c}$
O_{4c2}[111]	8	$2O_{vac}+2O_{4c}$	16	$2O_{vac}+2O_{4c}$
O_{4c3}[100]	2	$O_{vac}+O_{4c}$	10	$O_{vac}+O_{4c}$
O_{4c3}[110]	25	$3O_{vac}+3O_{4c}$	22	$4O_{vac}+4O_{4c}$
O_{4c3}[111]	6	$2O_{vac}+2O_{4c}$	11	$2O_{vac}+2O_{4c}$
O_{16h}[100]	22	$O_{vac}+O_{4c}$	34	$4O_{vac}+3O_{4c}+O_{int}$
O_{16h}[110]	4	$2O_{vac}+2O_{4c}$	11	$3O_{vac}+3O_{4c}$
O_{16h}[111]	1	$O_{vac}+O_{4c}$	19	$3O_{vac}+3O_{4c}$

4. Discussion

4.1. Formation enthalpy of $A_2Zr_2O_7$ (A = Gd, Lu) weberites

To gain deeper insight into the structural stability of the pyrochlore, defect-fluorite, and weberite phases, the formation enthalpies were evaluated based on the reaction [17]:

$$A_2O_3 + 2ZrO_2 \rightarrow A_2Zr_2O_7$$

Where A represents Gd or Lu. Following Ushakov et al. [78] and Rustad et al. [79], the C-type cubic structure was adopted for the heavier lanthanides from Eu to Lu. To correct for the known deficiency of standard DFT functionals in describing the phase stability of lanthanide oxides, which incorrectly predict C-type oxides as the most stable across the entire lanthanide series, the energies of these oxides were adjusted by +17.6 kJ/mol [17].

Comparison of the calculated formation enthalpies among the pyrochlore, defect-fluorite, and weberite phases provides additional evidence for their relative structural stability, consistent with the stability trend of weberite obtained from AIMD simulations in Section 3.1. The computed formation enthalpies are compared with available experimental and theoretical data in Fig. 9. The results reproduce the experimental formation enthalpies well for most compositions, with deviations from previous DFT results typically within 10 kJ/mol [17] and differences from experimental data generally within 30 kJ/mol [80].

Previous DFT studies have shown that defect-fluorite $Ln_2Zr_2O_7$ and $Ln_2Hf_2O_7$ phases exhibit large positive formation enthalpies, indicating their thermodynamically instability. In contrast, the weberite phase displays lower formation enthalpies than pyrochlore for compositions where disordered pyrochlore is experimentally observed as the stable phase [17,80]. Specifically for $Ln_2Zr_2O_7$, the weberite structure becomes more stable than pyrochlore when the A-site lanthanide is heavier than Gd, which is consistent with the present formation enthalpy results. The formation enthalpies of weberite and pyrochlore for $Gd_2Zr_2O_7$ are nearly identical, differing by only about 2 kJ/mol, consistent with previous DFT data [17].

The measured formation enthalpy of $Gd_2Zr_2O_7$ weberite is negative and the lowest among the three phases. This finding confirms that the disordered fluorite is not a completely random structure and that the weberite-type short-range ordering serves as a more realistic representation of the defect-fluorite phase. Overall, these results validate the use of the weberite configuration to describe $Gd_2Zr_2O_7$ and $Lu_2Zr_2O_7$ in this study.

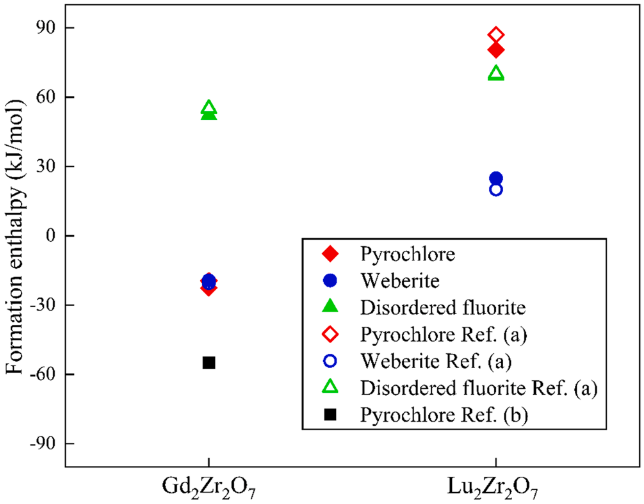

Fig. 9. The calculated formation enthalpies for $Gd_2Zr_2O_7$ and $Lu_2Zr_2O_7$ in pyrochlore (red diamonds), weberite (blue circles), and defect fluorite (green triangles) structures with available Refs.: (a) [17], (b) [80]. Ref. [17] is the source of DFT data for $Gd_2Zr_2O_7$ and $Lu_2Zr_2O_7$ oxides (hollow shape), Ref. [80] is the source for the experimental data on $Gd_2Zr_2O_7$ pyrochlore (black squares).

4.2. Influence of He doping at different interstitial sites on the structural and electronic properties of $A_2Zr_2O_7$ (A = Gd, Lu) weberites

The incorporation of He induces lattice expansion in the pyrochlore structure [50]. Table 2 shows that the incorporation of He leads to structural distortion. Interestingly, the lattice expansion in $Lu_2Zr_2O_7$ weberite is smaller than in $Gd_2Zr_2O_7$ weberite, indicating that the $Lu_2Zr_2O_7$ structure is less affected by the incorporation of He. $Lu_2Zr_2O_7$ weberite exhibits enhanced resistance to He-induced structural distortion. This phenomenon may originate from the smaller ionic radius of Lu^{3+} relative to Gd^{3+}, which strengthens the lattice framework and mitigates local strain caused by He incorporation, which might contribute to the relative stability of the $Lu_2Zr_2O_7$ framework.

In the He-$A_2Zr_2O_7$ (A = Gd, Lu) weberites, except for He-doped A_{8g}-A_{8g} interstitial sites, the He interstitials at other positions tend to relax and migrate toward the octahedral sites. The preferential migration of He interstitials toward octahedral sites (excluding A_{8g}-A_{8g} positions) highlights the role of site-specific energetics in governing He behavior. Octahedral sites likely provide a lower-energy configuration due to their coordination geometry, which minimizes lattice distortion.

We further calculated the Bader charges for both the pure and He-doped $A_2Zr_2O_7$ (A = Gd, Lu) weberite systems, with the average Bader charges for Gd and Zr summarized in Table 7. Compared to the pure $Gd_2Zr_2O_7$ weberite, the Bader charges of both Gd and Zr in the He-$Gd_2Zr_2O_7$ weberite generally increased, indicating a stronger ionic character in the $\langle$Gd-O$\rangle$ and $\langle$Zr-O$\rangle$ bonds. The ionic nature of the chemical bonds is closely related to the amorphization resistance of pyrochlore [65], as compounds with strong ionic bonds tend to be more resistant to amorphization under irradiation [30]. In contrast, stronger covalent bonding makes radiation-induced damage more prone to accumulation, increasing the likelihood of amorphization. From this perspective, the weaker covalent character introduced by He doping enhances the irradiation resistance of the $Gd_2Zr_2O_7$ weberite. However, in $Gd_2Zr_2O_7$ pyrochlore, He doping enhances the covalent character of $\langle$Gd-O$\rangle$ bonds while diminishing $\langle$Zr-O$\rangle$ bond covalency. Defect formation energy analyses reveal the $\langle$Zr-O$\rangle$ exhibits superior influence over irradiation resistance compared to $\langle$Gd-O$\rangle$ interactions in these systems [64]. In comparison to pure $Lu_2Zr_2O_7$ weberite, the Bader charges of Lu and Zr in the He-$Lu_2Zr_2O_7$ weberite exhibit minor fluctuations: the Bader charge of Lu decreases, indicating stronger covalency in the $\langle$Lu–O$\rangle$ bond, while the Bader charge of Zr increases, suggesting weaker covalency in the $\langle$Zr–O$\rangle$ bond. According to the calculation results of cation antisite defect formation energy in the subsequent sections, these findings imply that in the He-$Lu_2Zr_2O_7$ weberite, the $\langle$Zr–O$\rangle$ bond may play a more critical role in irradiation resistance than the $\langle$Lu–O$\rangle$ bond. Only based on these findings, we infer that $Gd_2Zr_2O_7$ weberite exhibits enhanced irradiation resistance compared to both $Gd_2Zr_2O_7$ pyrochlore and $Lu_2Zr_2O_7$ weberite.

It is worth noting that these differences between $Gd_2Zr_2O_7$ and $Lu_2Zr_2O_7$ weberites are strongly influenced by the lanthanide contraction effect [12,13]. The significantly smaller ionic radius of Lu^{3+} (0.977 Å for CN = 8) compared to Gd^{3+} (1.053 Å for CN = 8) results in a more compact lattice framework, shorter $\langle$Lu–O$\rangle$ bond lengths, and stronger cation-oxygen interactions. This compactness reduces lattice polarizability and limits the extent of local strain upon He incorporation, thereby suppressing defect generation and migration under irradiation. Consequently, the $Lu_2Zr_2O_7$ weberite exhibits higher intrinsic resistance to structural distortion and radiation damage than its Gd-containing counterpart, independent of He effects.

Table 7
Average Bader charges of A and Zr in $A_2Zr_2O_7$ (A = Gd, Lu) weberite systems and He-$A_2Zr_2O_7$ (A = Gd, Lu) weberite systems.

Average Bader charge (|e|)	$Gd_2Zr_2O_7$ weberite	He-$Gd_2Zr_2O_7$ weberite											
		Gd_{4b}-Gd_{4b}	Gd_{8g}-Gd_{8g}	Gd_{8g}-Gd_{4b}	Zr_{4a}-Zr_{4a}	Zr_{8g}-Zr_{8g}	Zr_{8g}-Zr_{4a}	O_{16h}-O_{4c1}	O_{16h}-O_{4c2}	O_{16h}-O_{4c3}	O_{16h}-O_{16h}	Oct.1	Oct.2
Gd	2.079	2.082	2.076	2.081	2.083	2.084	2.083	2.084	2.083	2.083	2.083	2.081	2.084
Zr	2.548	2.557	2.547	2.556	2.561	2.538	2.551	2.553	2.55	2.559	2.552	2.559	2.559

Average Bader charge (|e|)	$Lu_2Zr_2O_7$ weberite	He-$Lu_2Zr_2O_7$ weberite											
		Lu_{4b}-Lu_{4b}	Lu_{8g}-Lu_{8g}	Lu_{8g}-Lu_{4b}	Zr_{4a}-Zr_{4a}	Zr_{8g}-Zr_{8g}	Zr_{8g}-Zr_{4a}	O_{16h}-O_{4c1}	O_{16h}-O_{4c2}	O_{16h}-O_{4c3}	O_{16h}-O_{16h}	Oct.1	Oct.2
Lu	2.111	2.109	2.095	2.108	2.111	2.106	2.113	2.108	2.11	2.109	2.108	2.106	2.111
Zr	2.559	2.559	2.554	2.562	2.562	2.54	2.564	2.555	2.556	2.562	2.559	2.561	2.562

Average Bader charge (|e|)	$Gd_2Zr_2O_7$ pyrochlore [64].	He-$Gd_2Zr_2O_7$ pyrochlore			
		Gd-Gd	O-O	Oct	Tet
Gd	2.1625	2.162	2.158	2.158	2.159
Zr	2.5660	2.570	2.570	2.570	2.569

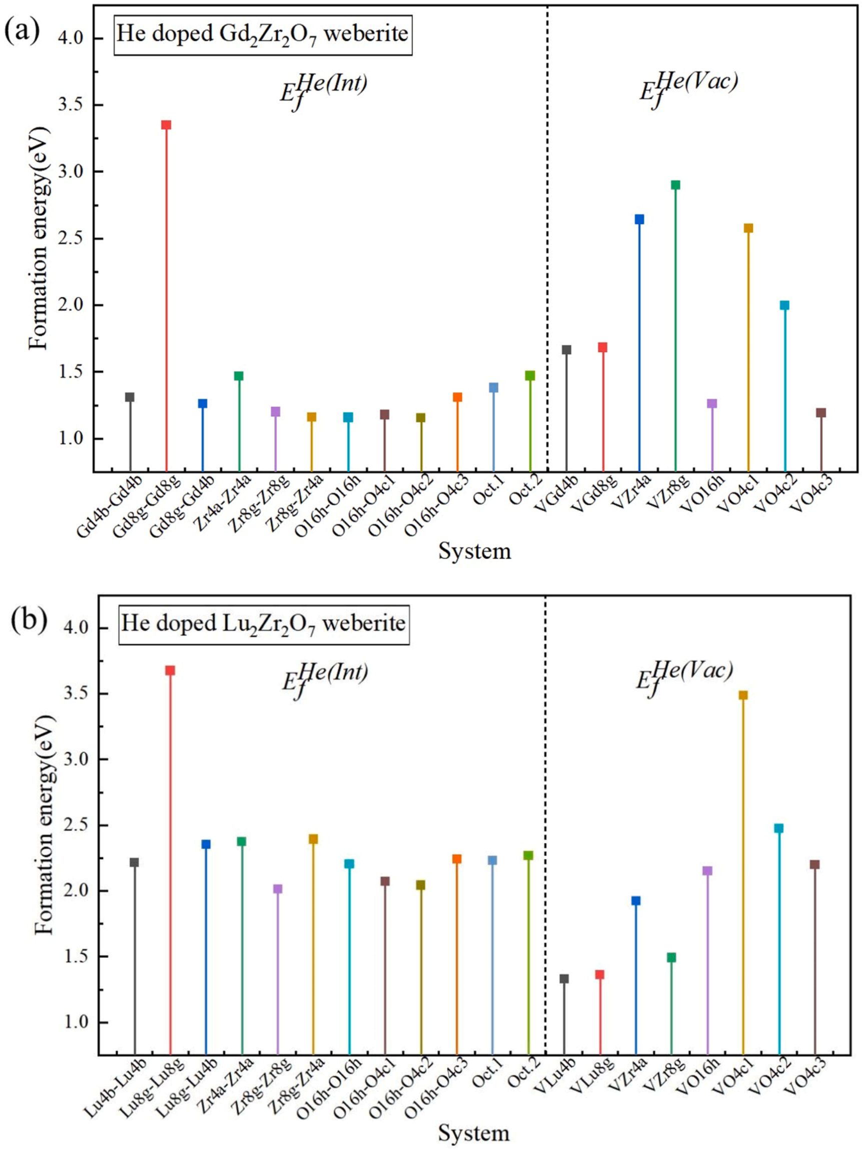

Fig. 10. (a) The formation energy of He atoms at different interstitial positions in $Gd_2Zr_2O_7$ weberite $E_f^{He(Int)}$ and pre-existing vacancy positions $E_f^{He(Vac)}$; (b) The formation energy of He atoms at different interstitial positions in $Lu_2Zr_2O_7$ weberite $E_f^{He(Int)}$ and pre-existing vacancy positions $E_f^{He(Vac)}$.

4.3. Preferable location of He in $A_2Zr_2O_7$ (A = Gd, Lu) weberites

A lower formation energy indicates stronger structural stability of the system [25,65–70]. As indicated in Table 3 and Fig. 10, The higher the formation energy of He in the $A_2Zr_2O_7$ (A = Gd, Lu) weberites, the more difficult it is for He to occupy the existing vacancies or interstitial sites. The trend derived from formation energy calculations is consistent with the results presented in Table 3. The calculated formation energies for He in $Gd_2Zr_2O_7$ weberite range from 1.155 to 3.353 eV at interstitial sites and from 1.194 to 2.9 eV at vacancy sites. Similarly, for $Lu_2Zr_2O_7$ weberite, the formation energies are 2.014–3.676 eV at interstitial sites and 1.331–3.488 eV at vacancy sites. These values are comparable to DFT-reported formation energies for He in other pyrochlore oxides. For example, in $Gd_2Zr_2O_7$ pyrochlore, formation energies are 0.979–1.424 eV at interstitial sites and 0.152–1.281 eV at vacancy sites [64]. In $La_2Zr_2O_7$ pyrochlore, they are 1.6–2.69 eV and 0.33–3.11 eV for interstitial and vacancy sites, respectively [65]. Similarly, in $La_2Sn_2O_7$ pyrochlore, the ranges are 1.33–2.93 eV and 0.45–2.23 eV [74], and in $Y_2Ti_2O_7$, 0.863–1.593 eV at interstitial sites [25]. The lowest formation energy is observed for a single He atom at the octahedral interstitial site in weberite structures. This trend is also consistent in the aforementioned pyrochlores. Compared to $Gd_2Zr_2O_7$ pyrochlore, where the formation energy for He at the octahedral interstitial site is the lowest (0.979 eV), the formation energies for He at interstitial sites in $Gd_2Zr_2O_7$ weberite are generally higher. Similarly, the formation energies for He at vacancy sites in $Gd_2Zr_2O_7$ pyrochlore are lower than those in $Gd_2Zr_2O_7$ weberite [64]. This is related to the difference in the local tectonic environment of weberite and pyrochlore. In the pyrochlore structure, the higher symmetry and larger free volume surrounding vacancy sites allow for greater local lattice relaxation upon He incorporation, reducing the energetic penalty [25,65,66]. In contrast, the orthorhombic weberite structure has a more compact lattice, stronger anisotropy in cation-oxygen coordination, and reduced polarizability, which restrict vacancy relaxation and increase the He formation energy. Lattice polarizability reflects the ability of a crystal lattice to redistribute its electronic charge and adjust ionic positions in response to local perturbations, such as point defects. Higher polarizability facilitates defect-induced local relaxation, thereby lowering defect formation energies. Due to the lanthanide contraction, Lu^{3+} has a significantly smaller ionic radius than Gd^{3+}, leading to a more compact electron cloud and reduced polarizability. This lower polarizability in the $Lu_2Zr_2O_7$ weberite limits the extent of vacancy relaxation upon He incorporation, resulting in higher He formation energies compared to the more polarizable $Gd_2Zr_2O_7$ pyrochlore. The results also suggest that He atoms are less likely to be trapped in interstitial or vacancy sites in $Gd_2Zr_2O_7$ weberite compared to the pyrochlore structure and the reduced trapping propensity may enhance radiation resistance by limiting He accumulation and subsequent bubble formations.

The consistently higher He formation energies in $Lu_2Zr_2O_7$ weberite compared to $Gd_2Zr_2O_7$ weberite (about 1 eV across most sites) can be attributed to the lanthanide contraction effect [12]. The smaller ionic radius of Lu^{3+} results in a more compact lattice and reduced interstitial free volume, which increases short-range repulsion and limits local structural relaxation upon He incorporation. Additionally, the lower lattice polarizability of $Lu_2Zr_2O_7$ further hampers the screening of the perturbation introduced by He atoms, thereby elevating the incorporation energy.

Furthermore, the elevated formation energies at A_{8g}-A_{8g} interstitial sites correlate with their structural instability, as large volume distortions destabilize these positions. The preferential migration of He toward octahedral sites aligns with their lower energy configuration, likely due to favorable coordination geometry that minimizes lattice strain, a behavior also observed in pyrochlores [64]. This suggests a universal energetic preference for He occupation in octahedral environments across related crystal structures. The formation energies for He in $Lu_2Zr_2O_7$ weberite are generally higher than those in $Gd_2Zr_2O_7$ weberite, suggesting that He incorporation is even more difficult in the $Lu_2Zr_2O_7$ weberite.

4.4. Binding energy and cation antisite defect formation energy

The binding energy serves as an indicator of the interaction intensity between particles in the system, a negative binding energy indicates that He atoms tend to form stable clusters at these sites, whereas a positive binding energy suggests that clustering at the given interstitial positions is energetically unfavorable [72]. Based on the binding energy data for two He atoms in Table 4, the simultaneous incorporation of two He atoms into A_{8g}-A_{8g} interstitial sites exhibits the lowest formation energy, with values of -4.252 eV for Gd_{8g}-Gd_{8g} and -3.967 eV for Lu_{8g}-Lu_{8g}. For other sites, the binding energies fluctuate around approximately 0 eV. Furthermore, when two He atoms are introduced into the same A_{8g}-A_{8g} interstitial site, atomic interactions cause them to relax into two adjacent octahedral interstitial positions. The large negative binding energy observed at this site is associated with the double occupancy of geometrically constrained, large-volume interstitial channels. This configuration significantly reduces local lattice distortion when two He atoms occupy adjacent positions compared to isolated ones. This phenomenon is consistent with observations in other oxide systems. For instance, He atoms in UO_2 are intrinsically repulsive, favoring uniform dispersion within the lattice over dimer formation. The most stable configuration involves two He atoms occupying separate, distant octahedral interstitial sites [81,82]. Similarly, in ThO_2, the energy-minimized configuration is achieved when two He atoms occupy independent, adjacent octahedral interstitial sites [83]. Moreover, as mentioned earlier, single He atoms at other interstitial sites invariably relax to octahedral center positions during structural optimization. This implies that the preferential occupation of He in weberites even at energetically favorable sites does not facilitate He clustering, as the structural framework inherently resists localized aggregation. Consequently, the weberite structure can only accommodate He at low concentrations, effectively suppressing He bubble formation. This unique property enhances its resistance to radiation-induced swelling and ensures long-term chemical stability under He accumulation conditions. This suggests that the structural characteristics of the weberite framework play a significant role in determining He aggregation behavior, possibly due to flexible coordination environments or charge redistribution. The notably large negative binding energies at the A_{8g}-A_{8g} positions are attributed to favorable elastic relaxation and charge redistribution effects within the weberite framework. When two He atoms are introduced into this channel-like site, the surrounding cation-anion sublattice undergoes cooperative adjustment, leading to a substantial reduction in the total elastic energy compared to the isolated single-He case. This results in a strongly exothermic binding process [25]. Furthermore, this demonstrates that the favorable elastic relaxation and charge redistribution effects are more pronounced in the relatively open and anisotropic A_{8g}-A_{8g} channel than in other interstitial environments. These synergistic effects collectively contribute to the significantly enhanced He binding affinity observed at these specific sites.

With cation antisite defect formation energy values for $Gd_2Zr_2O_7$ weberite ranging from -2 eV to 1.78 eV (Fig. 7 (a)), significantly lower than the 2.08 eV observed in $Gd_2Zr_2O_7$ pyrochlore [50]. This demonstrates exceptional tolerance to cation antisite defects in $Gd_2Zr_2O_7$ weberite, where low-energy-barrier defect formation facilitates controlled disordering to dissipate irradiation energy and mitigate damage accumulation [11,14,60]. This originates from the lower symmetry and more complex crystallographic environment of weberite versus pyrochlore [19,50]. Such complexity enables diverse atomic migration pathways and defect response mechanisms.

The incorporation of He significantly impacts the formation energy of cation antisite defects, as evidenced by the dependence of defect stability on He interstitial positions, which underscores the role of local lattice distortions induced by He doping. For instance, the stabilization of A (4b)-Zr (8 g) defects at Zr_{8g}-Zr_{8g} He sites may originate from strain relief via cation exchange, alleviating steric constraints imposed by He occupation. Similarly, the preference for Lu (8 g)-Zr (8 g) defects at O_{16h}-O_{4c2} He sites likely reflects charge compensation effects between He-induced oxygen sublattice perturbations and cation rearrangements. The negative formation energies observed at A_{8g}-A_{8g} He sites indicate spontaneous cation disordering under these conditions. This phenomenon aligns with the self-healing mechanism observed in radiation-tolerant materials, where defect formation promotes dynamic lattice recovery under irradiation [66]. The reduced antisite defect formation energies in He-doped weberites compared to undoped systems suggest that He incorporation lowers energy barriers for defect migration or recombination, thereby potentially enhancing damage tolerance. Additionally, the formation energies of cation antisite defects in the He-$A_2Zr_2O_7$ (A = Gd, Lu) weberite systems are lower than those in the undoped $A_2Zr_2O_7$ (A = Gd, Lu) weberite systems [11]. This suggests that He incorporation enhances irradiation resistance, making the He doped $A_2Zr_2O_7$ (A = Gd, Lu) weberites exhibits superior performance under radiation compared to pure weberite.

$Lu_2Zr_2O_7$ weberite exhibits higher cation antisite defect formation energy values (-1.52 eV to 2.58 eV) than $Gd_2Zr_2O_7$ weberite (Fig. 7 (b)), indicating greater energy barriers for anti-site defect formation and a thermodynamic preference for structural order. This disparity is fundamentally attributed to differences in A-site rare-earth ionic radii due to the lanthanide contraction effect [12,13]. The smaller Lu^{3+} ions in $Lu_2Zr_2O_7$ induce a denser, more strained lattice, where any antisite defect introduces substantial local strain, requiring higher energy to compensate for lattice distortion and resulting in elevated cation antisite defect formation energy values.

4.5. Displacement energies in $A_2Zr_2O_7$ (A = Gd, Lu) weberites

The threshold displacement energy is closely related to the radiation resistance of material [37,76]. Tables 5 and 6 summarize the E_d for PKAs of Gd, Lu, Zr and O in $A_2Zr_2O_7$ (A = Gd, Lu) weberites along the principal crystallographic directions and the corresponding defect configurations. This can be seen from the results that anion E_d values are significantly lower than cation E_d values, indicating that anion disorder, particularly between O_{16h} and O_{4c}, plays a dominant role in displacement events. This aligns with prior AIMD simulations of E_d in $Gd_2Zr_2O_7$ pyrochlore [51]. A key finding in $Gd_2Zr_2O_7$ weberite is that oxygen atoms not only preferentially occupy intrinsic vacancies at the 4c sites under low-energy recoil conditions but also tend to settle at the bridge sites along $\langle 001 \rangle$ between two Zr_{8g} atoms. This unique behavior, absent in $Lu_2Zr_2O_7$ weberite, suggests that this structural characteristic plays a crucial role in the order-disorder transition in $Gd_2Zr_2O_7$ weberite. Sickafus *et al.* systematically investigated the radiation resistance of complex oxides and suggested that compounds with more similar cation radii are more likely to transition into a disordered fluorite structure, exhibiting enhanced radiation resistance [15]. This may explain the formation of a special dumbbell structure during low-energy recoil events in $Gd_2Zr_2O_7$ weberite. Due to the low symmetry (orthogonal structure) of the weberite structure, the E_d value is highly dependent on the crystal direction and site type, and some directions (e.g., O_{16h} [111] = 1 eV) become the preferred channel for irradiation damage $Gd_2Zr_2O_7$ and $Lu_2Zr_2O_7$ weberites are strongly affected by the shrinkage effect of lanthanides [12,13]. Compared to Gd^{3+}, Lu^{3+} has a significantly smaller ion radius, resulting in a sparse $Gd_2Zr_2O_7$ weberite lattice framework, longer <Gd-*O*>bond length, and relatively weak cation-oxygen interaction. This makes it easier for O to break through the migration energy barrier, and the special dumbbell structure with the two adjacent Zr_{8g} makes it easier to generate defects and migration under irradiation. Furthermore, the A-site cation demonstrates greater displacement susceptibility relative to Zr, aligning with the conclusions drawn from AIMD simulations of the E_d values in $Gd_2Zr_2O_7$ pyrochlore [51]. The E_d for Gd at 4b and 8 g sites in $Gd_2Zr_2O_7$ weberite are significantly lower than those in pyrochlore [51], indicating enhanced Gd disorder in weberite likely due to distorted coordination polyhedra reducing binding energy. While Ed values for Zr at 4a and 8 g sites in $Gd_2Zr_2O_7$ weberite are generally lower than in pyrochlore, the difference is less pronounced [51]. This suggests that certain Gd and Zr sites exhibit higher disorder in weberite, likely arising from coordination polyhedra distortion weakening atomic binding. However, Zr site stability remains largely unaffected by structural type. In contrast, oxygen E_d values differ substantially between $Gd_2Zr_2O_7$ weberite and pyrochlore, attributed to the complex coordination environments of oxygen sites in weberite, which promote metastable configurations and higher susceptibility to displacement, accelerating oxygen sublattice disordering. In low energy recoil events, the typical types of defects generated are Frenkel pairs or cation antisite defects. Comparative analysis of $Gd_2Zr_2O_7$ weberite and $Lu_2Zr_2O_7$ weberite structures reveals that cation antisite defects exhibit a higher formation propensity in $Gd_2Zr_2O_7$ weberite compared to $Lu_2Zr_2O_7$ weberite, which is consistent with the previous conclusions. Additionally, cations and anions exhibit higher susceptibility to displacement in $Gd_2Zr_2O_7$ weberite, as nearly all E_d values are lower than in $Lu_2Zr_2O_7$ weberite, except for Gd_{4b}[111] and O_{4c3}[110], which are slightly higher. This suggests that $Gd_2Zr_2O_7$ weberite is more prone to order-disorder phase transitions than $Lu_2Zr_2O_7$ weberite. Considering its defect formation energies, $Gd_2Zr_2O_7$ weberite may exhibit enhanced radiation damage resistance. Moreover, a comparison of the E_d values between $Gd_2Zr_2O_7$ weberite and $Gd_2Zr_2O_7$ pyrochlore demonstrates that the weberite phase may enhance radiation resistance relative to its pyrochlore structure.

4.6. Comparison with existing studies

A wide range of studies have investigated defect energetics, threshold displacement energies, and irradiation tolerance in pyrochlore and defect fluorite structures. Experimental measurements and atomistic computer simulation consistently show that the cation antisite defect formation energy is a critical descriptor of radiation resistance, as lower energies facilitate defect recombination and delay amorphization [15,33,84]. However, it is important to note that the disordering of the anion sublattice is also a significant factor in the structural evolution. First-principles studies by Li et al. [85] suggest that oxygen diffusion resulting from the formation of Frenkel defect pairs can be a primary factor driving the O-D transition. Due to their relatively low E_d, oxygen atoms exhibit high mobility and are prone to displacement to participate in local structural relaxation under irradiation [37]. Previous studies have emphasized that oxygen disorder is largely coupled with cation rearrangements rather than independently driving the O-D transition [86]. Molecular dynamics simulations and first-principles calculations have shown that cation antisite formation serves as the primary driving force for disordering, while the anion sublattice follows and accommodates the structural distortions induced by cationic disorder [33,86,87]. Such cation-anion coupling allows the oxygen sublattice to accommodate charge redistribution and lattice relaxation during irradiation-induced disordering. Studies on PKA threshold displacement energies indicate that anion E_d values are substantially smaller than cation E_d values, with oxygen atoms being the most mobile species in pyrochlore under irradiation [37,51]. In comparing ordered pyrochlore and disordered defect fluorite phases, defect fluorite structures often exhibit higher amorphization resistance due to enhanced structural flexibility and reduced energy penalty for disordering, allowing for more efficient accommodation of point defects [15]. Our findings are consistent with these observations, showing that the ease of cation antisite formation influence the radiation response, with structural symmetry and lattice compactness further modulating these effects.

5. Conclusions

First-principles density functional theory calculations have been used to investigate the structural and electronic properties of $A_2Zr_2O_7$ (A = Gd, Lu) weberites, including cation antisite defect formation energies. The results indicate that cation antisite defects form more easily in weberite compared to pyrochlore. Further analysis of He-doped $A_2Zr_2O_7$ (A = Gd, Lu) weberites shows reveals that He incorporation generally leads to lattice expansion, increasing both lattice constants and overall volume. The formation energy analysis indicates that, except for He interstitials at the A_{8g}-A_{8g} site, He atoms at other interstitial positions preferentially relax into octahedral sites, highlighting a strong tendency for octahedral interstitial occupation. An increase in the concentration of He at various interstitial sites reveals that He does not readily cluster in $A_2Zr_2O_7$ (A = Gd, Lu) weberites. Additionally, the incorporation of He reduces cation antisite defect formation energies in the $A_2Zr_2O_7$ (A = Gd, Lu) weberites, promoting a transition from ordered to disordered phases. Bader charge analysis shows that the ⟨Zr-O⟩ bond has a more significant effect on the irradiation resistance of the He-$Lu_2Zr_2O_7$ weberite compared to the ⟨Lu-O⟩ bond, while both ⟨Gd-O⟩ and ⟨Zr-O⟩ bonds jointly influence the irradiation resistance in the He-$Gd_2Zr_2O_7$ weberite. To systematically assess and compare the irradiation resistance of $Gd_2Zr_2O_7$ weberite and $Lu_2Zr_2O_7$ weberite, the low-energy recoil phenomena were analyzed using AIMD simulations. The results demonstrate that E_d exhibits strong directional dependence, with anion disorder playing a more prominent role in displacement events. Additionally, anions preferentially occupy intrinsic vacancy sites at the 4c positions, and the A-site cations are more susceptible to displacement than Zr cations. In low-energy recoil events, cation antisite defects are generated more easily in $Gd_2Zr_2O_7$ weberite than in $Lu_2Zr_2O_7$ weberite, aligning with the observed trends in cation antisite defect formation energies. Compared to $Gd_2Zr_2O_7$ pyrochlore, $Gd_2Zr_2O_7$ weberite exhibits generally lower threshold displacement energies than both $Lu_2Zr_2O_7$ weberite and $Gd_2Zr_2O_7$ pyrochlore. Under low-energy irradiation, $Gd_2Zr_2O_7$ weberite is more susceptible to undergo order-disorder phase transitions than $Lu_2Zr_2O_7$ weberite and $Gd_2Zr_2O_7$ pyrochlore. Based on the defect formation energy analysis, these findings suggest that $Gd_2Zr_2O_7$ weberite exhibits superior radiation resistance.

CRediT authorship contribution statement

Xiaoyi Xia: Writing – original draft, Formal analysis, Investigation. **Haowen Guo:** Formal analysis. **Rongrong Gao:** Formal analysis. **Yue Xia:** Formal analysis, Investigation. **Chenguang Liu:** Writing – review & editing, Supervision, Funding acquisition, Formal analysis, Conceptualization. **Qing Peng:** Formal analysis, Investigation. **Yuhong Li:** Writing – review & editing. **Fei Gao:** Writing – review & editing.

Declaration of competing interest

The authors declare that they have no known competing financial interests or personal relationships that could have appeared to influence the work reported in this paper.

Acknowledgements

This work is supported by the National Natural Science Foundation of China (Grant No. 12205248), Shandong Provincial Natural Science Foundation (Grant No. ZR2024MA065, ZR2021QA028, ZR2023MA045), the start-up fund from Yantai University to C.L. (Grant No. HD20B02.), and Key Laboratory of Advanced Nuclear Energy Technology Design and Safety Ministry of Education (Grant No. KLA-NETDS-KF-202412).

Supplementary materials

Supplementary material associated with this article can be found, in the online version, at doi:10.1016/j.jnucmat.2026.156624.

Data availability

Data will be made available on request.

References

[1] S.A. McMaster, R. Ram, N. Faris, M.I. Pownceby, Radionuclide disposal using the pyrochlore supergroup of minerals as a host matrix—A review, J. Hazard. Mater. 360 (2018) 257–269.

[2] L. Yang, C. Zhu, Y. Sheng, H. Nian, Q. Li, P. Song, W. Lu, J. Yang, B. Liu, Investigation of mechanical and thermal properties of rare earth pyrochlore oxides by first-principles calculations, J. Am. Ceram. Soc. 102 (5) (2019) 2830–2840.

[3] F. Li, L. Zhou, J.-X. Liu, Y. Liang, G.-J. Zhang, High-entropy pyrochlores with low thermal conductivity for thermal barrier coating materials, J. Adv. Ceram. 8 (2019) 576–582.

[4] G. Sattonnay, N. Sellami, L. Thomé, C. Legros, C. Grygiel, I. Monnet, J. Jagielski, I. Jozwik-Biala, P. Simon, Structural stability of $Nd_2Zr_2O_7$ pyrochlore ion-irradiated in a broad energy range, Acta Mater. 61 (17) (2013) 6492–6505.

[5] A. Shlyakhtina, L. Shcherbakova, New solid electrolytes of the pyrochlore family, Russ. J. Electrochem. 48 (2012) 1–25.

[6] T. Jiang, F. Wu, Y. Ren, J. Qiu, Z. Chen, Pyrochlore phase $(Y,Dy,Ce,Nd,La)_2Sn_2O_7$ as a superb anode material for lithium-ion batteries, J. Solid State Electrochem. 27 (3) (2023) 763–772.

[7] A.A.A. Ali, S. Acharya, K. Bhongale, S. Shirbhate, S. Kulkarni, S. Joshi, Investigation of Sr doping effect on oxygen ion de-localization in $Gd_2Ti_2O_7$ pyrochlore system and its influence on charge relaxation dynamics and ionic conductivity: as electrolyte for IT-SOFCs, Ion (Kiel) 30 (11) (2024) 7293–7310.

[8] A.E. Ringwood, S.E. Kesson, N. Ware, W. Hibberson, A. Major, Immobilisation of high level nuclear reactor wastes in SYNROC, Nature 278 (5701) (1979) 219–223.

[9] R.C. Ewing, W.J. Weber, J. Lian, Nuclear waste disposal—Pyrochlore ($A_2B_2O_7$): nuclear waste form for the immobilization of plutonium and "minor" actinides, J. Appl. Phys. 95 (11) (2004) 5949–5971.

[10] N. Gumber, M. Shafeeq, S.K. Gupta, R. Phatak, U.K. Goutam, R. Kumar, R.V. Pai, Synthesis and feasibility studies of doping U at Ti site of $Y_2Ti_2O_7$ as a radioactive waste immobilization matrix, Dalton Trans. 52 (39) (2023) 14170–14181.

[11] Y. Li, B.P. Uberuaga, C. Jiang, S. Choudhury, J.A. Valdez, M. Patel, J. Won, Y.-Q. Wang, M. Tang, D.J. Safarik, Role of antisite disorder on preamorphization swelling in titanate pyrochlores, Phys. Rev. Lett. 108 (19) (2012) 195504.

[12] J. Lian, K. Helean, B. Kennedy, L. Wang, A. Navrotsky, R. Ewing, Effect of structure and thermodynamic stability on the response of lanthanide stannate pyrochlores to ion beam irradiation, J. Phys. Chem. B 110 (5) (2006) 2343–2350.

[13] M. Subramanian, G. Aravamudan, G.S. Rao, Oxide pyrochlores—A review, Prog. Solid State Chem. 15 (2) (1983) 55–143.

[14] K.E. Sickafus, R.W. Grimes, J.A. Valdez, A. Cleave, M. Tang, M. Ishimaru, S. M. Corish, C.R. Stanek, B.P. Uberuaga, Radiation-induced amorphization resistance and radiation tolerance in structurally related oxides, Nat. Mater. 6 (3) (2007) 217–223.

[15] K. Sickafus, L. Minervini, R. Grimes, J.A. Valdez, M. Ishimaru, F. Li, K.J. Mcclellan, T. Hartmann, Radiation tolerance of complex oxides, Science 289 (5480) (2000) 748–751.

[16] S. Finkeldei, P. Kegler, P. Kowalski, C. Schreinemachers, F. Brandt, A. Bukaemskiy, V. Vinograd, G. Beridze, A. Shelyug, A. Navrotsky, Composition dependent order-disorder transition in $Nd_xZr_{1-x}O_{2-0.5x}$ pyrochlores: a combined structural, calorimetric and ab initio modeling study, Acta Mater. 125 (2017) 166–176.

[17] P.M. Kowalski, Formation enthalpy of $In_2B_2O_7$-type (B= Ti, Sn, Hf, Zr) compounds, Scr. Mater. 189 (2020) 7–10.

[18] J. Shamblin, M. Feygenson, J. Neuefeind, C.L. Tracy, F. Zhang, S. Finkeldei, D. Bosbach, H. Zhou, R.C. Ewing, M. Lang, Probing disorder in isometric pyrochlore and related complex oxides, Nat. Mater. 15 (5) (2016) 507–511.

[19] F. Zhao, S. Hu, C. Xu, H. Xiao, X. Zhou, X. Zu, S. Peng, Probing local site disorder in zirconate pyrochlores, Ceram. Int. 49 (11) (2023) 18432–18441.

[20] U. Matsumoto, T. Ogawa, S. Kitaoka, H. Moriwake, I. Tanaka, First-principles study on the stability of weberite-type, pyrochlore, and defect-fluorite structures of $A_2^{3+}B_2^{4+}O_7$ (A= Lu^{3+}–La^{3+}, B= Zr^{4+}, Hf^{4+}, Sn^{4+}, and Ti^{4+}), J. Phys. Chem. C 124 (37) (2020) 20555–20562.

[21] B. Mandal, M. Pandey, A. Tyagi, $Gd_2Zr_2O_7$ pyrochlore: potential host matrix for some constituents of thoria based reactor's waste, J. Nucl. Mater. 406 (2) (2010) 238–243.

[22] S.-X. Wang, B. Begg, L.-M. Wang, R. Ewing, W. Weber, K.G. Kutty, Radiation stability of gadolinium zirconate: a waste form for plutonium disposition, J. Mater. Res. 14 (12) (1999) 4470–4473.

[23] F. Zhao, Y. Tian, Z. Teng, S. Hu, Effect of short-range order on the solubility of actinides in $Gd_2Zr_2O_7$, Ceram. Int. (2024).

[24] W.J. Weber, R.C. Ewing, C. Catlow, T.D. De La Rubia, L.W. Hobbs, C. Kinoshita, A. Motta, M. Nastasi, E. Salje, E. Vance, Radiation effects in crystalline ceramics for the immobilization of high-level nuclear waste and plutonium, J. Mater. Res. 13 (6) (1998) 1434–1484.

[25] T. Danielson, C. Hin, Structural and electronic effects of helium interstitials in $Y_2Ti_2O_7$: a first-principles study, J. Nucl. Mater. 452 (1–3) (2014) 189–196.

[26] T. Danielson, E. Tea, C. Hin, Ab initio investigation of helium in $Y_2Ti_2O_7$: mobility and effects on mechanical properties, J. Nucl. Mater. 477 (2016) 215–221.

[27] B. Begg, N. Hess, D. McCready, S. Thevuthasan, W. Weber, Heavy-ion irradiation effects in $Gd_2(Ti_{2-x}Zr_x)O_7$ pyrochlores, J. Nucl. Mater. 289 (1–2) (2001) 188–193.

[28] M. Glerup, O.F. Nielsen, F.W. Poulsen, The structural transformation from the pyrochlore structure, $A_2B_2O_7$, to the fluorite structure, AO_2, studied by Raman spectroscopy and defect chemistry modeling, J. Solid State Chem. 160 (1) (2001) 25–32.

[29] M. Robinson, N. Marks, K. Whittle, G. Lumpkin, Systematic calculation of threshold displacement energies: case study in rutile, Phys. Rev. B—Condens. Matter Mater. Phys. 85 (10) (2012) 104105.

[30] K. Trachenko, Understanding resistance to amorphization by radiation damage, J. Phys.: Condens. Matter 16 (49) (2004) R1491.

[31] J. Nord, K. Nordlund, J. Keinonen, Molecular dynamics study of damage accumulation in GaN during ion beam irradiation, Phys. Rev. B 68 (18) (2003) 184104.

[32] G. Lucas, L. Pizzagalli, Ab initio molecular dynamics calculations of threshold displacement energies in silicon carbide, Phys. Rev. B—Condens. Matter Mater. Phys. 72 (16) (2005) 161202.

[33] A. Chartier, C. Meis, J.-P. Crocombette, W.J. Weber, L.R. Corrales, Molecular dynamic simulation of disorder induced amorphization in pyrochlore, Phys. Rev. Lett. 94 (2) (2005) 025505.

[34] H. Xiao, F. Gao, X.T. Zu, W.J. Weber, Threshold displacement energy in GaN: ab initio molecular dynamics study, J. Appl. Phys. 105 (12) (2009).

[35] G. Lucas, L. Pizzagalli, Comparison of threshold displacement energies in β-SiC determined by classical potentials and ab initio calculations, Nucl. Instrum. Methods Phys. Res. B: Beam Interact. Mater. At. 229 (3–4) (2005) 359–366.

[36] H.Y. Xiao, F. Gao, W.J. Weber, Threshold displacement energies and defect formation energies in $Y_2Ti_2O_7$, J. Phys.: Condens. Matter 22 (41) (2010) 415801.

[37] H.Y. Xiao, W.J. Weber, Y. Zhang, X. Zu, Ab initio molecular dynamics simulations of ion–solid interactions in zirconate pyrochlores, Acta Mater. 87 (2015) 273–282.

[38] S. Mohan, G. Kaur, C. David, B. Panigrahi, G. Amarendra, Ab initio molecular dynamics simulation of threshold displacement energies and defect formation energies in $Y_4Zr_3O_{12}$, J. Appl. Phys. 127 (23) (2020).

[39] F. Gao, H. Xiao, X. Zu, M. Posselt, W.J. Weber, Defect-enhanced charge transfer by ion-solid interactions in SiC using large-scale ab initio molecular dynamics simulations, Phys. Rev. Lett. 103 (2) (2009) 027405.

[40] G. Kresse, J. Furthmüller, Efficient iterative schemes for ab initio total-energy calculations using a plane-wave basis set, Phys. Rev. B 54 (16) (1996) 11169.

[41] G. Kresse, J. Furthmüller, Efficiency of ab-initio total energy calculations for metals and semiconductors using a plane-wave basis set, Comput. Mater. Sci. 6 (1) (1996) 15–50.

[42] P.E. Blöchl, Projector augmented-wave method, Phys. Rev. B 50 (24) (1994) 17953.

[43] G. Kresse, D. Joubert, From ultrasoft pseudopotentials to the projector augmented-wave method, Phys. Rev. B 59 (3) (1999) 1758.

[44] J.P. Perdew, K. Burke, M. Ernzerhof, Generalized gradient approximation made simple, Phys. Rev. Lett. 77 (18) (1996) 3865.

[45] F. Zhao, H. Xiao, Z. Liu, S. Li, X. Zu, A DFT study of mechanical properties, thermal conductivity and electronic structures of Th-doped $Gd_2Zr_2O_7$, Acta Mater. 121 (2016) 299–309.

[46] F. Zhao, H. Xiao, X. Bai, Z. Liu, X. Zu, Effects of doping Yb^{3+}, La^{3+}, Ti^{4+}, Hf^{4+}, Ce^{4+} cations on the mechanical properties, thermal conductivity, and electronic structures of $Gd_2Zr_2O_7$, J. Alloys Compd. 776 (2019) 306–318.

[47] G. Lan, B. Ouyang, J. Song, The role of low-lying optical phonons in lattice thermal conductance of rare-earth pyrochlores: a first-principle study, Acta Mater. 91 (2015) 304–317.

[48] E.C. O'Quinn, K.E. Sickafus, R.C. Ewing, G. Baldinozzi, J.C. Neuefeind, M. G. Tucker, A.F. Fuentes, D. Drey, M.K. Lang, Predicting short-range order and correlated phenomena in disordered crystalline materials, Sci. Adv. 6 (35) (2020) eabc2758.

[49] A. Zunger, S.-H. Wei, L.G. Ferreira, J.E. Bernard, Special quasirandom structures, Phys. Rev. Lett. 65 (3) (1990) 353.

[50] C. Liu, R. Gao, Y. Xia, X. Xia, T. Shi, Q. Peng, F. Gao, Y. Li, A comparative first-principles study on the physical properties of $Gd_2Zr_2O_7$ weberite and pyrochlore, Comput. Mater. Sci. 245 (2024) 113285.

[51] X. Wang, H.Y. Xiao, X. Zu, Y. Zhang, W.J. Weber, Ab initio molecular dynamics simulations of ion–solid interactions in $Gd_2Zr_2O_7$ and $Gd_2Ti_2O_7$, J. Mater. Chem. C 1 (8) (2013) 1665–1673.

[52] K. Momma, F. Izumi, VESTA: a three-dimensional visualization system for electronic and structural analysis, J. Appl. Crystallogr. 41 (3) (2008) 653–658.

[53] A. Stukowski, Visualization and analysis of atomistic simulation data with OVITO–the Open Visualization Tool, Model. Simul. Mater. Sci. Eng. 18 (1) (2009) 015012.

[54] C. Liu, Q. Peng, T. Shi, F. Gao, Y. Li, Physical properties and radiation tolerance of high-entropy pyrochlores $Gd_2(Ti_{0.25}Zr_{0.25}Sn_{0.25}Hf_{0.25})_2O_7$ and individual pyrochlores $Gd_2X_2O_7$ (X= Ti, Zr, Sn, Hf) from first principles calculations, Scr. Mater. 220 (2022) 114898.

[55] X. Zhang, H. Zhao, S. Gao, Q. Zeng, First-principles study of electronic structure and optical properties of Er: lu_2O_3, J. Rare Earths 39 (4) (2021) 453–459.

[56] J. Feng, B. Xiao, C. Wan, Z. Qu, Z. Huang, J. Chen, R. Zhou, W. Pan, Electronic structure, mechanical properties and thermal conductivity of $ln_2Zr_2O_7$ (Ln= La, Pr, Nd, Sm, Eu and Gd) pyrochlore, Acta Mater. 59 (4) (2011) 1742–1760.

[57] F. Zhao, H. Xiao, X. Bai, Z. Liu, X. Zu, Effects of Nd doping on the mechanical properties and electronic structures of $Gd_2Zr_2O_7$: a first-principles-based study, J. Mater. Sci. 53 (24) (2018) 16423–16438.

[58] J. Lian, X. Zu, K.G. Kutty, J. Chen, L. Wang, R. Ewing, Ion-irradiation-induced amorphization of $La_2Zr_2O_7$ pyrochlore, Phys. Rev. B 66 (5) (2002) 054108.

[59] L. Minervini, R.W. Grimes, K.E. Sickafus, Disorder in pyrochlore oxides, J. Am. Ceram. Soc. 83 (8) (2000) 1873–1878.

[60] G. Henkelman, A. Arnaldsson, H. Jónsson, A fast and robust algorithm for Bader decomposition of charge density, Comput. Mater. Sci. 36 (3) (2006) 354–360.

[61] E. Sanville, S.D. Kenny, R. Smith, G. Henkelman, Improved grid-based algorithm for Bader charge allocation, J. Comput. Chem. 28 (5) (2007) 899–908.

[62] W. Tang, E. Sanville, G. Henkelman, A grid-based Bader analysis algorithm without lattice bias, J. Phys.: Condens. Matter. 21 (8) (2009) 084204.

[63] A.D. Becke, K.E. Edgecombe, A simple measure of electron localization in atomic and molecular systems, J. Chem. Phys. 92 (9) (1990) 5397–5403.

[64] C. Zhu, B. Ding, D. Yang, Y. Li, C. Liu, Comparative study on the radiation resistance of pure and He-doped $Gd_2Zr_2O_7$ pyrochlore by DFT+ U calculation, Nucl. Instrum. Methods Phys. Res. B: Beam Interact. Mater. At. 516 (2022) 8–14.

[65] C. Liu, Y. Li, Y. Li, L. Dong, J. Wen, D. Yang, Q. Wei, P. Yang, First principle calculation of helium in $La_2Zr_2O_7$: effects on structural, electronic properties and radiation tolerance, J. Nucl. Mater. 500 (2018) 72–80.

[66] L. Yang, Y. Jiang, G. Robert Odette, T. Yamamoto, Z. Liu, Y. Liu, Trapping helium in $Y_2Ti_2O_7$ compared to in matrix iron: a first principles study, J. Appl. Phys. 115 (14) (2014).

[67] B. Tsuchiya, T. Yamamoto, K. Ohsawa, G. Odette, First-principles calculation of formation energies and electronic structures of hydrogen defects at tetrahedral and octahedral interstitial sites in pyrochlore-type $Y_2Ti_2O_7$ oxide, J. Alloys Compd. 678 (2016) 153–159.

[68] Y.-L. Liu, L. Wang, K.J. Yang, P. Shao, Influence of carbon on hydrogen retention in molybdenum for nuclear material application: a first-principles investigation, Nucl. Mater. Energy 33 (2022) 101311.

[69] K.J. Yang, Y.-L. Liu, H.-H. Li, P. Shao, X. Zhang, Q.-F. Han, Y. Ma, The early growth process of helium blistering in tungsten and molybdenum: first-principles and statistical model calculations, J. Nucl. Mater. 550 (2021) 152938.

[70] K.J. Yang, Y.-L. Liu, P. Shao, X. Zhang, Q.-F. Han, Y. Ma, First-principles simulation of h interacting with transition elements in molybdenum for nuclear material application, J. Nucl. Mater. 541 (2020) 152437.

[71] W.J. Weber, A. Navrotsky, S. Stefanovsky, E.R. Vance, E. Vernaz, Materials science of high-level nuclear waste immobilization, MRS Bull. 34 (1) (2009) 46–53.

[72] P. Zhang, C. Zhang, R. Li, J. Zhao, He-induced vacancy formation in bcc Fe solid from first-principles simulation, J. Nucl. Mater. 444 (1–3) (2014) 147–152.

[73] A.-Y. Gao, Y.-L. Liu, Z.-H. Dai, C. Duan, Elucidating hydrogen assisting vacancy formation in metals: Mo and Nb as examples, Eur. Phys. J. B 86 (2013) 1–8.

[74] X. Li, Y. Lu, Q. Peng, Y. Liu, K. Yang, C. Xu, F. Gao, Y. Li, C. Liu, Ab initio investigation of properties and mobility of helium defects in La2Sn2O7 pyrochlore, Nucl. Mater. Energy 30 (2022) 101135.

[75] W.R. Panero, L. Stixrude, R.C. Ewing, First-principles calculation of defect-formation energies in the $Y_2(Ti, Sn, Zr)_2O_7$ pyrochlore, Phys. Rev. B—Condens. Matter Mater. Phys. 70 (5) (2004) 054110.

[76] L. Dong, Y. Li, R. Devanathan, W. Setyawan, F. Gao, Low energy ion-solid interactions and chemistry effects in a series of pyrochlores, J. Am. Ceram. Soc. 100 (7) (2017) 3132–3144.

[77] R. Devanathan, W.J. Weber, Simulation of collision cascades and thermal spikes in ceramics, Nucl. Instrum. Methods Phys. Res. B: Beam Interact. Mater. At. 268 (19) (2010) 2857–2862.

[78] S. Ushakov, K. Helean, A. Navrotsky, L. Boatner, Thermochemistry of rare-earth orthophosphates, J. Mater. Res. 16 (9) (2001) 2623–2633.

[79] J.R. Rustad, Density functional calculations of the enthalpies of formation of rare-earth orthophosphates, Am. Mineral. 97 (5–6) (2012) 791–799.

[80] M. Saradhi, S. Ushakov, A. Navrotsky, Fluorite-pyrochlore transformation in $Eu_2Zr_2O_7$-direct calorimetric measurement of phase transition, formation and surface enthalpies, RSC Adv. 2 (8) (2012) 3328–3334.

[81] Y. Yun, O. Eriksson, P.M. Oppeneer, Theory of He trapping, diffusion, and clustering in UO_2, J. Nucl. Mater. 385 (3) (2009) 510–516.

[82] Y. Yun, O. Eriksson, P.M. Oppeneer, First-principles modeling of He-clusters in UO_2, J. Nucl. Mater. 385 (1) (2009) 72–74.

[83] N. Kuganathan, P. Ghosh, A. Arya, R. Grimes, Helium trapping and clustering in ThO_2, J. Nucl. Mater. 507 (2018) 288–296.

[84] S. Huang, J. Zhang, H. Fu, Y. Xiong, S. Ma, X. Xiang, B. Xu, W. Lu, Y. Zhang, W. J. Weber, Irradiation performance of high entropy ceramics: a comprehensive comparison with conventional ceramics and high entropy alloys, Prog. Mater. Sci. 143 (2024) 101250.

[85] Y.L. Piotr, M. Kowalski, George Beridze, April R. Birnie, Sarah Finkeldei, Dirk Bosbach, Defect formation energies in $A_2B_2O_7$ pyrochlores, Scr. Mater. 107 (2015) 18–21.

[86] V. Kocevski, G. Pilania, B. Uberuaga, Modeling disorder in pyrochlores and other anion-deficient fluorite structural derivative oxides, Front. Chem. 9 (2021) 1–10, 2021.

[87] C. Jiang, C.R. Stanek, K. Sickafus, B.P. Uberuaga, First-principles prediction of disordering tendencies in pyrochlore oxides, Phys. Rev. B—Conden. Matter Mater. Phys. 79 (10) (2009) 104203.